Renewable Electricity Generation via Solar-Powered Methanol Reforming: Hybrid Proton Exchange Membrane Fuel Cell Systems Based on Novel Non-Concentrating, Intermediate-Temperature Solar Collectors

by

Daniel J. Real

Department of Mechanical Engineering and Materials Science
Duke University

Date:_____

Approved:

_____
Nico Hotz, Supervisor

_____
Timothy L. Johnson

_____
Adrian Bejan

_____
Laurens E. Howle

_____
Walter Neal Simmons

Dissertation submitted in partial fulfillment of
the requirements for the degree of Doctor
of Philosophy in the Department of
Mechanical Engineering and Materials Science
in the Graduate School
of Duke University

2015

Abstract

Renewable Electricity Generation via Solar-Powered Methanol Reforming:

Hybrid Proton Exchange Membrane Fuel Cell Systems Based on Novel Non-

Concentrating, Intermediate-Temperature Solar Collectors

by

Daniel J. Real

Department of Mechanical Engineering and Materials Science
Duke University

Date:_____

Approved:

_____
Nico Hotz, Supervisor

_____
Timothy L. Johnson

_____
Adrian Bejan

_____
Laurens E. Howle

_____
Walter Neal Simmons

An abstract of a Dissertation submitted in partial
fulfillment of the requirements for the degree of
Doctor of Philosophy in the Department of
Mechanical Engineering and Materials Science
in the Graduate School of
Duke University
2015

Abstract

Tremendous research efforts have been conducted studying the capturing and conversion of solar energy. Solar thermal power systems offer a compelling opportunity for renewable energy utilization with high efficiencies and excellent cost-effectiveness. The goal of this work was to design a non-concentrating collector capable of reaching temperatures above 250 °C, use this collector to power methanol steam reforming, and operate a proton exchange membrane (PEM) fuel cell using the generated hydrogen. The study presents the construction and characterization of a non-concentrating, intermediate-temperature, fin-in-tube evacuated solar collector, made of copper and capable of reaching stagnation temperatures of 268.5 °C at 1000 W/m^2 irradiance. The collector was used to power methanol steam reforming, including the initial heating and vaporization of liquid reactants and the final heating of the gaseous reactants. A preferential oxidation (PROX) catalyst was used to remove CO from simulated reformate gas, and this product gas was used to operate a PEM fuel cell. The results show 1) that the outlet temperature is not limited by heat transfer from the absorber coating to the heat transfer fluid, but by the amount of solar energy absorbed. This implicates a constant heat flux description of the heat transfer process and allows for the usage of materials with lower thermal conductivity than copper. 2) It is possible to operate a PEM fuel cell from reformate gas if a PROX catalyst is used to remove CO

from the gas. 3) The performance of the fuel cell is only slightly decreased (~4%) by CO_2 dilution present in the reformate and PROX gas. These results provide a foundation for the first renewable electricity generation via solar-powered methanol reforming through a hybrid PEM fuel cell system based on novel non-concentrating, intermediate-temperature solar collectors.

Contents

List of Tables

List of Figures

Nomenclature

A_{coll}	Area of the collector absorber plate	m^2
A_{apt}	Area of light aperture	m^2
A'_{ij}	Intermolecular energy exchange parameter between components i and j	
C	Coefficient	
$C_{m/GDL}$	Water capacity of the membrane/GDL	kg
$C_{p,l}$	Specific heat of liquid	J/(kg·K)
$C_{p,v}$	Specific heat of vapor	J/(kg·K)
$D_{i/o}$	Pipe inner/outer diameter	m
ΔH	Total enthalpy rate	W
ΔH_{vap}	Specific heat of vaporization	J/kg
h	Convective heat transfer coefficient	W/(m²·K)
$\bar{h}_{liq/vap}$	Enthalpy of liquid and vapor methanol-water mixture	J/(mol·K)
$\bar{h}_{react}$	Enthalpy of methanol-steam reforming reaction	J/(mol·K)
I	Incident solar irradiance	W/m^2
k^*	Thermal conductivity of mixed gas	W/(m·K)
k_i	Thermal conductivity of component i	W/(m·K)
k'_i	Mixture adjusted thermal conductivity of component i	W/(m·K)
k_f	Thermal conductivity of fluid	W/(m·K)

k_s	Thermal conductivity of solid porous material	W/(m·K)
k_G	Thermal conductivity of fluid in porous medium, geometric mean	W/(m·K)
$\dot{L}_{Prod/Out}$	Rate of water production/removal	kg/s
L	Length	m
L_b	Bulkhead thickness	m
M_i	Molecular mass of species i	g/mol
$\dot{m}$	Mass flow rate	kg/s
Nu_{D_i}	Nusselt number based on D_i	
$\dot{n}_{in/out}$	Molar inlet/outlet flow rate	mol/s
$\dot{n}_{in,total}$	Molar inlet/outlet flow rate	mol/s
Q_{loss}	Heat losses	W
$Q_{loss,glass}$	Reflective and absorptive heat losses by glass	W
$Q_{reflect}$	Radiation reflected by the absorber plate	W
$Q_{emit,top}$	Radiation emitted from the top-side of the absorber	W
$Q_{emit,bottom}$	Radiation emitted from the bottom-side of the absorber	W
$Q_{loss,cond}$	Conductive heat losses	W
$Q_{loss,other}$	Remaining heat losses	W
Q_{solar}	Solar heat input	W
Q_{use}	Captured thermal energy	W

q''	Heat flux	W/m^2
R_b	Thermal resistance of the bulkhead	K/W
R_t	Thermal resistance of the tubing	K/W
S_i	Sutherland constant of species i	K
T_∞	Ambient temperature	K
T_b	Boiling temperature	K
$T_{b,o}$	Outside temperature of the bulkhead	K
T_{coll}	Collector temperature	K
T_g	Glass temperature	K
$T_{in/out}$	Inlet/outlet temperature	K
T_m	Mean temperature	K
ΔT_m	Difference in mean temperature	K
T_W	Wall temperature	K
t_0	Time corresponding to zero-power	s
t_{ideal}	Time corresponding to maximum power at a stable state	s
$t_{max\ power}$	Time corresponding to maximum power at an unstable state	s
v_i	Volume concentration of component i	
V_{steel}	Volume of steel wool fibers	m^3
V_{plug}	Volume of porous medium	m^3

Greek Symbols

α_{sol}	Absorptivity in the UV-Vis-NIR range
γ_{i}	Coefficient
δ	Adjustment parameter for η
ε_{IR}	Emissivity in the IR
η	Process state parameter
η_{chem}	Chemical efficiency
η_i	Initial value of η
$\eta_{i,ideal}$	Initial value of η that will reach an ideal stable state
η_{ref}	Methanol conversion
$\eta_{solar-\mathrm{H_2}}$	Solar-to-hydrogen efficiency
η_{therm}	Thermal efficiency
$\eta_{thermocat}$	Thermocatalytic efficiency
κ	Ratio of adjusted thermal conductivities
σ	Stefan-Boltzmann constant ..... $5.67{\cdot}10^{-8}\ \mathrm{W/(m^2 \cdot K^4)}$)
σ_{i}	Collision diameter of species i.....m
τ_g	Transmissivity of glass
ϕ	Void fraction
$\phi_{i,flooded}$	Fraction of GDL that is pre-flooded
$\phi_{i,dried}$	Fraction of membrane that is pre-dried

Acronyms

CL Catalyst Layer

EOD Electro-osmotic Drag

ETC Evacuated tube collector

FPC Flat-plate collector

FSP Flame spray pyrolysis

GC Gas Chromatograph

GCR Geometric concentration ratio

GDL Gas Diffusion Layer

IR Infrared

I-V Current-Voltage

LHV Lower heating value

MEA Membrane Electrode Assembly

MPL Micro-porous Layer

NRTL Non-random two-liquid

OCV Open Circuit Voltage

ORR Oxygen Reduction Reaction

PEM Proton exchange membrane

PROX preferential oxidation

PTC Parabolic trough collector

PV	Photovoltaic
SEM	Scanning electron micrograph
SMR	Steam molar ratio
STP	Standard Temperature and Pressure
TEM	Transmission electron micrograph

1. Introduction

Modern society consumes much of its available, and often non-renewable, resources at an astonishing rate. While society debates how much longer we can sustain such consumption, scientists are developing new technologies based on renewable resources that will be a necessity in the future. One very promising field of research is the efficient capture of solar energy through solar thermal systems. The aim of this document is to present the current state of research into the design, manufacture, and characterization of a novel non-concentrating, intermediate-temperature solar thermal collector for renewable hydrogen production by solar-powered methanol reforming; and, a hybrid proton exchange membrane (PEM) fuel cell system based on such a collector.

This research can be easily separated into three phases. In the first phase, the performance and characteristics of the solar collector were explored in detail. This analysis has been published in the journal *Solar Energy* [1]. The second phase of testing introduced the methanol reforming catalyst into the solar collector. The relationship between fuel flow rate, catalyst mass, and hydrogen production was explored, and the successful production of hydrogen from methanol confirmed the feasibility of solar-heated fuel reforming. The journal article demonstrating the results of these experiments has been submitted for publication [2]. The third phase examined the combined preferential oxidation (PROX) and PEM fuel cell system needed to clean and use the

produced hydrogen for electricity generation. The production, characterization and effectiveness of the PROX catalyst has been examined in detail by Shodiya et. al. [3], and is not the focus of this document. Instead, the effect of the resultant gas on the power output of the fuel cell, along with best practices for the operation of the fuel cell are discussed. These topics, along with improvements to the PROX catalyst after the submission of [3] are presented in a journal article that is currently in preparation. The following document is constructed largely from passages taken from these three publications.

In section 2, a review of existing technologies relevant to the research is presented; beginning, with an historical overview of solar thermal collector design, and the state of research into fuel cell operation. Section 2.1 establishes the multiple types of solar thermal collectors and compares their pros and cons. The current applications of solar thermal collectors are discussed, and new applications are suggested.

Then, a discussion of hydrogen, as an energy carrier, is presented, beginning in section 2.2. Current methods of traditional hydrogen generation and novel solar-based methanol steam reforming are discussed, and their disadvantages described.

Section 2.3 presents the current theory behind the operation of PEM fuel cells, with a focus on water management inside the fuel cell. The effect of humidity and liquid water on power output is explained. The consequences of poor water management are also described.

Finally, the idea of a non-concentrating solar thermal collector as the hydrogen generator in a fully integrated reforming fuel cell system is presented as a dramatic improvement to current solutions.

In section 3, experimental equipment and, where necessary, their construction are detailed. The detailed description of the design and manufacture of the solar collector is the aim of section 3.1. The reasoning behind material choice and design is presented, and the desired performance characteristics are described. Section 3.2 provides details on the preparation of the $CuO/ZnO/Al_2O_3$ nanoparticle catalyst used during hydrogen production experiments. A brief characterization of the catalyst is also presented. The vacuum system used in the operation of the solar collector is described in section 3.3. The preparation of the nano-scale $Au/\alpha\text{-}Fe_2O_3$ PROX catalyst along with a brief characterization is presented in section 3.4. Finally, the PEM fuel cell and accompanying gas humidification system, along with the combined PROX-PEM fuel cell system are described in sections 3.5 and 3.6.

Experimental testing consisted of the three phases mentioned previously, design and evaluation of the solar collector, methanol-steam reforming within the solar collector, and combing the PROX and PEM fuel cell systems. The experimental procedures of each phase are presented in section 4. Testing equipment used in the first two phases pertaining to the solar collector can be found in section 4.1. Testing equipment used during the characterization of the solar collector can be found in section

4.2. Testing equipment used during the production of hydrogen via methanol-steam reforming can be found in section 4.3. Operation of the PROX and PEM fuel cell individually and combined can be found in section 4.4.

Sections 5 and 6 provide the analytical foundation of the thesis. First the definition of solar collector efficiency is described and modified to account for boiling of the heat transfer fluid. Then, section 6 presents the analytical model used to describe the performance of the solar collector. This analysis accounts for the modified thermal conductivity of the vapor mixture, and the effect of porous media on heat transfer.

Section 7 describes a conceptual model for the practical operation of a PEM fuel cell. The model conjectures that performance of the fuel cell can be generalized to a mass balance between the water transfer mechanisms on the cathode side gas diffusion layer of the fuel cell. Based on that conjecture, predictions are made as to the behavior of the fuel cell under a variety of operating conditions. These predictions are intended to provide experimentalists an intuition for the behavior of a fuel cell.

Section 8 presents the results for each phase of experimental testing, and a discussion of the findings from the analytical and conceptual models. First in section 8.1, the solar collector is analyzed on its own merit. Then, after the addition of the catalyst, the effectiveness of the system for hydrogen production is discussed in section 8.2. The findings of the heat transfer analysis on the solar collector are presented in section 8.3 Section 8.4 analyses the affect of CO_2 dilution on the performance of a PEM fuel cell. The

performance of the hybrid PROX-PEM fuel cell system can be found in section 8.5. Finally, the implications for best water management practices based on the conceptual model for the behavior of the fuel cell, along with some experimental validation of these practices are presented in section 8.6.

The major conclusions of the current work are offered in section 9.

2. Current State-of-the-Art

2.1 Historical Overview of Solar Thermal Collectors

Enormous research efforts have been conducted to find better ways to capture solar energy to meet the growing energy demands of the modern world. Solar energy is clean, renewable, abundant, and easily captured. Photovoltaic (PV) cells are one of the most popular ways to capture solar energy, but their relatively low efficiency and high cost have impeded wide-spread use [4]. Furthermore, there is concern over the limited availability of high-quality silicon produced for traditional silicon PV cells [5]. Solar thermal power systems offer a compelling alternative with efficiencies above 40% [6, 7], and excellent cost-effectiveness among renewable energy sources [8-10].

Systems for collecting solar thermal power can be categorized broadly into two groups: concentrating and non-concentrating. Concentrating collectors typically use mirrored surfaces to focus light from a large area to a smaller area where the absorber material is located. By comparison, non-concentrating systems directly absorb light which is incident on their surface [6].

In a concentrating collector, the ratio of the collector area to the absorber area is known as the geometric concentration ratio (GCR). Parabolic trough collectors (PTCs), the most common type of concentrating collector, typically have GCRs of 15-30 and can reach temperatures of 300-400 °C [6, 9, 11-14]. There are, however, disadvantages associated with PTCs and any other concentrating collector. They require large

concentration ratios in order to reach high temperatures, and as the concentration ratio increases, the collector's field of view decreases [11]. This renders diffuse light less and less effective [6, 11]. Using only direct sunlight requires complex and expensive sun-tracking systems [6, 9, 11], and causes the system to be inoperable during inclement weather. The reflective surfaces used by PTCs can also degrade over time [6], particularly in the sandy desert conditions where they are commonly operated.

Of the two broad categories, concentrating and non-concentrating collectors, numerous subtypes of collectors can be defined by their geometry and method of thermal insulation. The simplest and most common non-concentrating solar collector design is the flat-plate collector (FPC). As the name suggests, these collectors use a flat absorber surface to capture light. They transfer heat to a working fluid, and use traditional insulation materials such as foam or fiberglass to retain heat. FPCs are commonly found in residential applications, being well suited to provide thermal energy for water and space heating. However, high thermal losses prevent these systems from operating efficiently above 100 °C [6, 7, 11, 15].

Previous research has shown that thermal losses could be reduced by replacing conventional insulation materials with a moderate vacuum [15, 16]. This eliminated, or at least reduced, convective losses from the absorber to its enclosure and raised the operational temperatures to 150 °C at 45% efficiency [15, 17]. These higher temperatures allowed FPCs to be used for absorptive cooling, industrial steam-processing and

commercial hot water. To the best knowledge of the author, the performance of FPCs has not been improved above 150 °C.

Unfortunately, the design of these evacuated FPCs remains problematic. Sealing the large perimeter of the system and supporting the large flat cover characteristic of a FPC are very difficult. As such, the design has had limited commercial success [11]. In 1979, several companies, e.g., Corning Glass Works [11], abandoned the difficult flat-plate geometry and created evacuated collectors with tubular geometries. These tubular designs had the inherent structural rigidity to contain moderate and potentially higher vacuum. The design also greatly reduced the length of seals, moving them only to the entrance and exit of the tube. Such a design appeared in scientific literature as early as 1965 [8].

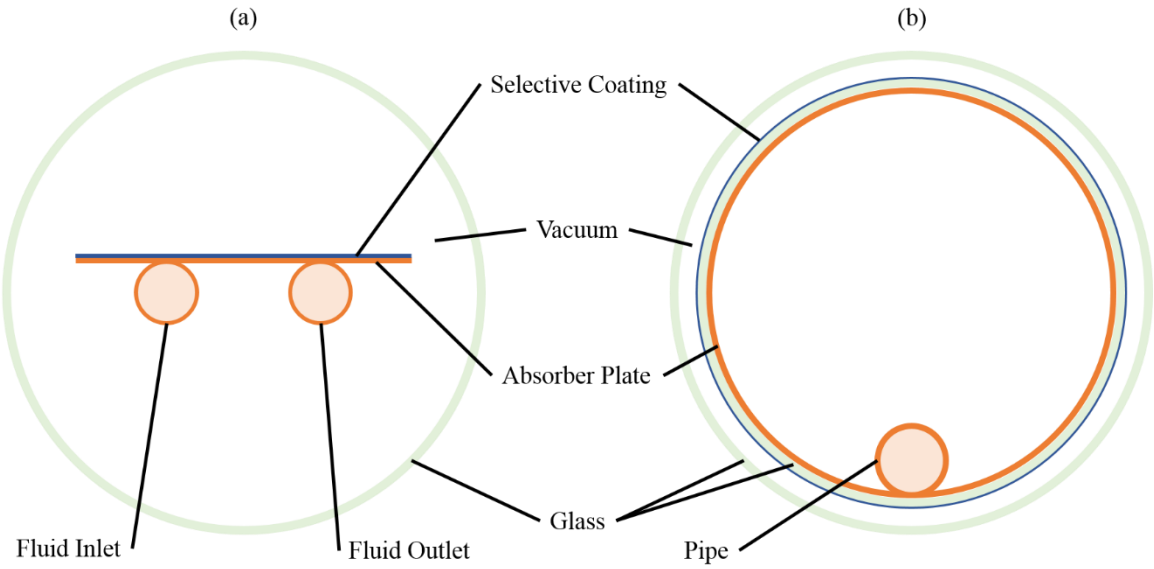

Figure 1: The most common evacuated tube collector (ETC) designs are the fin-in-tube (a) and Sydney tube designs (b).

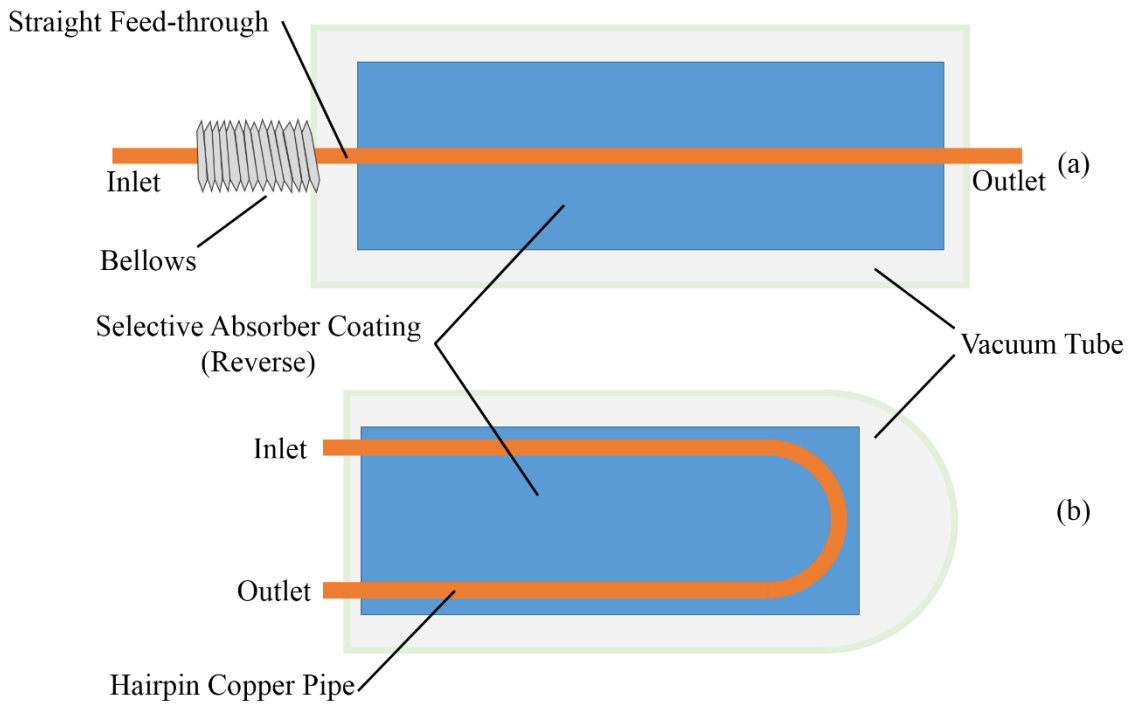

Figure 2: Fin-in-tube designs used a flat absorber surface with an attached tube that either passed through the glass housing (a), or looped back in a hairpin (b).

These first evacuated tube collectors (ETCs) had a "fin-in-tube" design similar to FPCs (Fig. 1a). They used a flat absorber surface with an attached tube that either passed through the glass housing (Fig. 2a) or looped back in a hairpin (Fig. 2b). Straight feed-through designs as shown in Figure 2a avoid the thermal short circuit that is created in the proximity of the inlet and outlet tubes in looped designs such as Figure 2b; however, they are more difficult to manufacture, since they require a bellows seal to accommodate the thermal expansion of the collector relative to the glass. An alternative design called Sydney tube (Fig. 1b) used an absorber plate and selective coating applied to a glass

tube, which was then encased by a second glass tube, with a vacuum in-between, creating a shape similar to a Dewar flask.

While these and other ETC designs have seen extensive use in industry, with at least fifty major manufacturers worldwide, e.g., Kingspan Solar and SolarMaxx [18], high temperature ETCs have never been thoroughly tested in scientific literature. To the best knowledge of the author, only one ETC system has demonstrated the capability of reaching operational temperatures well above 150 °C, reporting experimentally measured temperatures of 194 °C, from a theoretically predicted maximum of 220 °C using supercritical CO_2 [19, 20].

Non-concentrating, high-vacuum collectors able to achieve operational temperatures well above 150 °C have enormous, untapped functionality. Attaining such a high level of performance means high-temperature ETCs have the potential to power systems like organic Rankine cycles [21], intermediate-temperature fuel reforming [22-26], bio-fuel pre-treatment [23, 27], hydrolysis (e.g. to convert lignocellulosic biomass to ethanol) [23], esterification (e.g. to produce biodiesel) [23], and non-aqueous distillation processes [23]. A simple Carnot efficiency calculation for an ideal heat engine shows that increasing operating temperatures from 150 to 260 °C – for a standard ambient temperature of 25 °C – improves theoretical efficiencies by nearly one-half. Furthermore, a non-concentrating collector capable of achieving temperatures comparable with PTCs offers numerous auxiliary benefits. Non-concentrating collectors are easier to construct

and simpler to maintain because they do not require the complex tracking systems and delicate reflective surfaces of concentrating systems [6]. After installation, they are generally cost competitive with PTCs per irradiated area [11, 28]; and, because they can take advantage of indirect illumination, they are less dependent on the incident angle of incoming light and are less sensitive to inclement weather [6].

2.2 Hydrogen Production Methods

Hydrogen, as an energy carrier, has the potential to replace fossil fuels as the dominant form of fuel in the world's economy. Energy conversion technologies that run on hydrogen, like fuel cells, have the advantages of being clean and efficient. They have the ability to meet transient energy demands by simple and affordable gas storage, in contrast to renewable energy solutions based on solar or wind energy, which typically require expensive batteries for electric energy storage. However, an economically competitive and sustainable means of hydrogen production must be developed before any hydrogen-based economy can be considered seriously. There are currently two major industrial pathways to produce hydrogen, steam reforming of hydrocarbons and water electrolysis, with steam reforming of natural gas generating the substantial majority of the world's hydrogen. The steam reforming process requires large amounts of heat to evaporate the water and liquid fuel mixture, and drive the endothermic reaction, and the reformate gas contains byproducts toxic to PEM fuel cells. For the case of methanol steam reforming, for every 1 kWh of produced hydrogen (defined by its

lower heating value, LHV) approximately 1 kWh of thermal energy is required [22, 29]. Other hydrocarbon and alcoholic fuels lead to similar results. Currently, conventional fuel reforming systems generate this required heat by combusting 40-50% of the initial fuel and, therefore, convert only half of the fuel to hydrogen. This loss and the polluting byproducts of the combustion process render modern steam reforming neither clean nor efficient. Instead, an ideal solution would combine a heat source that preserves the entire fuel-feedstock, releases no harmful byproducts, and is freely available, with a method of removing components of the reformate gas toxic to PEM fuel cells. Due to the elevated temperatures for fuel reforming (e.g. ~250 °C for methanol steam reforming and above 500 °C for other alcoholic and higher hydrocarbon fuels), process waste heat is typically not an applicable heat source.

Solar thermal collectors, however, are sources of heat that are well-established, clean, and commonly convert solar irradiation to heat with over 40% efficiency [6, 7]. Extensive research has shown that traditional and non-traditional power plants could benefit greatly by integrating solar thermal collectors as heat sources [30-36]. These hybrid power plants have demonstrated exergetic efficiencies 5-10 percentage points higher than their non-solar counterparts in simulations [30-32]. A variety of solar thermal collectors have been suggested, depending on the proposed role in the power system. PTCs are typically used for fuel pre-heating and steam generation [30, 34-36], while solar power towers and parabolic dish concentrators are used for higher

temperature processes, such as molten salt heating [33], air superheating [34], methane membrane reforming [32], or biomass gasification in supercritical water [37]. However, due to high heat demands in all of these processes, only concentrating solar thermal collectors have been proposed for integration into traditional power plants.

Recent interest has turned toward upgrading lower-quality solar thermal energy to higher-quality chemical energy through thermocatalytic reactions [24, 31, 32, 37-45]. Methanol has stood out due to the relatively low temperatures required for its steam reforming. Many researchers have demonstrated the possibility to efficiently drive the endothermic steam reforming of methanol with solar heat from a PTC [24, 31, 38-41]. However, the solar collectors in these experiments have provided only the thermal energy for the reaction, while the fuel and water were evaporated and preheated by external (electrical) heaters before entering the collector. This evaporation and preheating accounts for the majority of the heating requirement, which is neglected by these studies. To the best knowledge of the author, no experiment has demonstrated steam reforming of methanol entirely sustained by a non-concentrating solar collector.

Unfortunately, PTCs and other concentrating systems require complex and expensive sun-tracking systems [6, 9, 11], are difficult to maintain [6], and require direct sunlight to operate [6, 11]. A simple non-concentrating system that can passively collect energy without the considerable expense and maintenance of a concentrating system would be preferable.

2.3 Water Management in PEM Fuel Cells

A PEM fuel cell (Fig. 3) uses input gases, hydrogen and oxygen, to generate electricity with heat and water as the resulting exhaust. The chemical reactions occur in the catalyst layer (CL) on the surface of the proton exchange membrane (Fig. 3 detail). Critical to the performance of the CL is the platinum catalyst found at the interface of the membrane and the gas diffusion layer (GDL) or micro-porous layer (MPL). Hydrogen is stripped of its electrons at the anode through the hydrogen oxidation reaction, and water is produced through the oxygen reduction reaction (ORR) at the cathode. While the protons are able to diffuse through the membrane, the electrons have to travel from the anode through an external circuit to reach the cathode, generating an external current.

$$H_2 \rightarrow 2H^+ + 2e^- \quad \text{(I)}$$

$$O_2 + 4H^+ + 4e^- \rightarrow 2H_2O \quad \text{(II)}$$

$$2H_2 + O_2 \rightarrow 2H_2O + \text{heat} \quad \text{(III)}$$

Most commonly, fuel cells are run with pure hydrogen and air, which is used to supply the oxygen.

Losses in PEM fuel cells come from four primary sources (Fig. 4). First, open circuit voltage (OCV) is reduced from reversible voltage by small amounts of fuel crossover and internal currents, i.e. minute electron conduction through the membrane

[46]. Second, voltage decreases quickly due to activation losses, which is the energy required to drive the reactions, and is essentially the voltage difference between the anode and cathode terminals [47]. Third, ionic and electric resistance in the membrane, electrodes and external circuit cause ohmic losses as charge moves through the system. The ohmic losses through the membrane can be greatly reduced through proper water management. Finally, as reactant is consumed by the cell, the concentration of available reactant decreases, causing concentration loss. Because this is in effect a failure to deliver sufficient reactant to the membrane, this is commonly referred to as mass transfer loss [46].

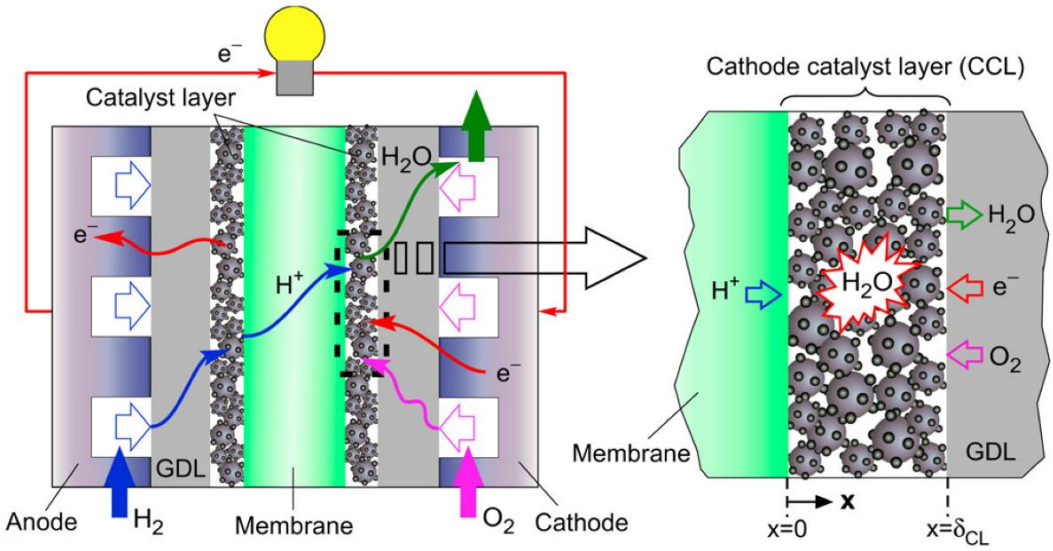

Figure 3: Basic PEM fuel cell schematic including detail of the cathode catalyst layer and its reactions [48].

Water management in PEM fuel cells comes from the desire to reduce the ohmic losses due to poor hydration of the membrane. It is important then to understand how

hydration effects the transport of protons from the anode to the cathode. Jiao and Li describe proton conductivity through the membrane along three pathways: 1) direct proton transport between sulphonated side chains, 2) by diffusing through the membrane as a hydrogen-water ion (such as H_3O^+), or 3) if there is enough water to provide a contiguous pathway between side chains, protons may jump from one water molecule to another. These last two processes are known as vehicular and structural diffusion respectively. Each of these three mechanisms becomes dominant for increasingly higher water content in the membrane and correspondingly reduce the ohmic losses of proton transport through the membrane [46]. These losses are strongly dependent on hydration, as proton conductivity by hydration has been shown to roughly follow the Arrhenius Law [49].

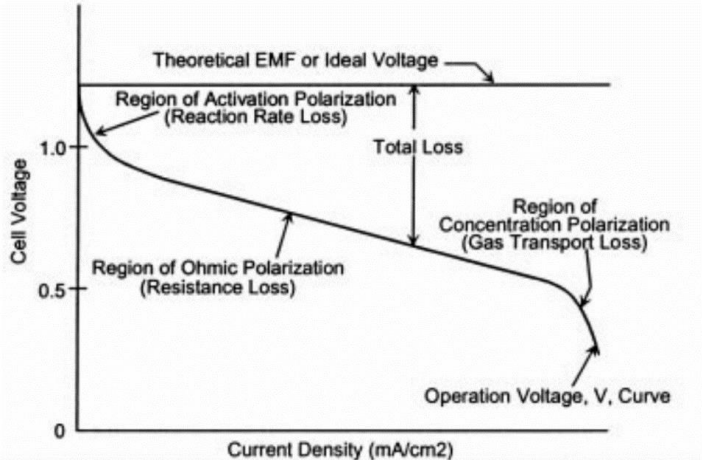

Figure 4: Representative schematic of the I-V curve of a PEM fuel cell [47]. Dominant losses are indicated for each portion of the curve.

It is clear then that minimizing the ohmic loss means maximizing membrane hydration; however, it is not possible to simply flood the system with liquid water or

water vapor. Doing so would block, or flood, the flow field and/or the GDL, thereby preventing the transport of reactant gases to the surface of the membrane. It is necessary then to provide enough water to the membrane to maintain its hydration, without oversupplying water, and blocking the flow of reactant gases. This goal of balancing hydration levels in the membrane with flooding in the flow field and GDL is the crux of water management research.

Water management is complicated by the five ways water migrates within the fuel cell. 1) It is introduced through condensation out of the humid fuel and oxidizing gas flows and leaves through evaporation with the exhaust gas flows. 2) It is produced at the cathode through the ORR. 3) It is dragged by the flow of protons from the anode to the cathode in a process called electro-osmotic drag (EOD). 4) It naturally diffuses from the area of high water concentration at the cathode to the typically dryer anode. This diffusion is called back-diffusion. Finally, 5) it is wicked through capillary forces throughout the flow field and GDL.

Humidity of the incoming reactant gas can be controlled through a variety of means; in research settings this is most commonly accomplished by sparging gases through liquid water. The temperature of the water can be adjusted to control the humidity of the exiting gases. The effect of EOD is largely dependent on the ionic current density [46]. Back diffusion can be enhanced by reducing the thickness of the membrane, but is ultimately constrained by the need for physical durability. Wicking

through the flow field and GDL can be influenced by numerous factors including the shape of the flow field, the relative orientations of the anode and cathode flow fields, the porosity of the GDL, the hydrophobicity of the GDL, and the presence or absence of a MPL between the membrane and GDL, just to name a few. The two most influential controls researchers have over water management in the fuel cell are adjustment of inlet gas humidity and the properties of the flow field and GDL. Controlling the inlet gas humidity is relatively straight forward and well understood, though still difficult to execute well. There is still much room for improvement in our understanding of how liquid water moves through the flow field and the GDL, and improving that understanding has become a particularly important aspect of water management research [48, 50-69].

The water transport mechanism inside the GDL and MPL can, at present, only be described by a combination of several theories. Predominant among them are the converging capillary tree mechanism, proposed by Nam and Kaviany [50], and Pasapgullari and Wang [51], and the fingering and channeling mechanism described by Litster et al. [52].

Further research has supported both of these mechanisms showing their occurrence is likely spatially dependent and occurs simultaneously [53]. Additionally, it has been shown that preferential pathways can be formed by cracks and other imperfections in the MPL and GDL [54, 55], thereby facilitating the channeling

mechanism. The author hypothesizes that the channeling mechanism is primarily responsible for the transport of water out of the most active areas of the cell, the catalyst layer and MPL in the cathode flow channel. In less active areas such as between flow channels, or in cells without a MPL, water transport is dominated by a capillary tree mechanism.

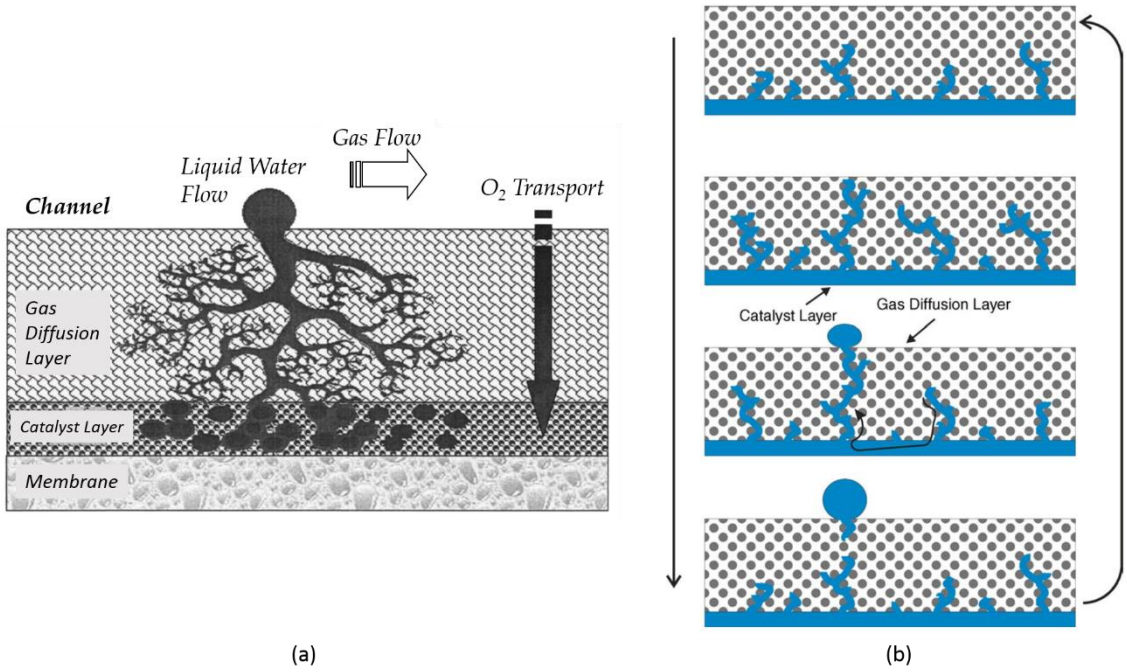

Figure 5: Water transport mechanisms with the GDL and MPL. (a) a converging capillary tree mechanism, proposed by Nam and Kaviany [50], and Pasapgullari and Wang [51]. (b) the fingering and channeling mechanism described by Litster et al. [52].

Additionally, cells operated at high temperature will likely see the capillary tree mechanism dominate throughout the cell due to the higher levels of vapor condensation in the GDL at high temperature gradients. However, as Lu describes, these capillary trees are likely interconnected and breakthrough events at one location will affect flow

in surrounding trees [55], effectively creating the channels described by Litster er al. [52], but with a tree rather than finger shape. The defining distinction between the channeling and capillary tree mechanisms seems to be the dominant source of water. If water is generated uniformly throughout the GDL, or at the GDL/MPL interface, the capillary tree mechanism will likely dominate. However, if the majority of water with the GDL enters through preferential pathways formed by imperfections in the MPL, then channeling will likely dominate.

The flow field itself has seen extensive research [56, 66-69]. There are currently three primary flow field shapes, parallel, serpentine, and interdigitated [46, 56, 70]. Parallel flow fields maintain a very small pressure drop across the cell, but are most susceptible to flooding [69]. Serpentine and interdigitated flow fields sacrifice an increase in pressure drop for improved water management characteristics [69]. Interdigitated flow fields are particularly interesting in that they do not provide a direct path from entrance to exit, but force gases to flow through the GDL. This greatly increases pressure drop across the cell, but facilitates water transport out of the GDL, and improves the supply of reactant gases to the membrane, leading to a 50-100% improvement in fuel cell performance over conventional designs [70].

2.4 Summary and Proposal

For the first time, this work presents experimental proof of methanol steam reforming within a non-concentrating solar thermal collector. This collector consists of

advanced selective solar absorber coatings; novel nanoparticle catalysts; and an efficient thermal design in the form of an evacuated fin-in-tube solar collector. This design, though well established in industry, had never been applied to operate at the high temperature required for in-situ steam reforming. This new solar-based steam reforming system is able to perform methanol steam reforming inside the solar collector and produces hydrogen with very high efficiency. These results make the first steps towards a sustainable and commercially viable source of thermocatalytically generated hydrogen from non-concentrated sunlight.

Furthermore, this study establishes the novel possibility of a successful direct combination of alcohol-steam reforming with PEM fuel cells by proving that a PROX catalyst can provide efficient CO removal between hydrogen generation and fuel cells. It is shown that the toxic products of methanol-steam reforming can be rendered harmless to a PEM fuel cell, and that non-toxic dilutants in the PROX product gas have very little effect on the performance of PEM fuel cells.

3. Materials and Construction

3.1 Solar Collector

3.1.1 Back-plate Assembly

A 10 x 10 cm^2 square plate of 0.8 mm thick Ultra Conductive Copper (alloy 101) was used as the support plate and 6.5 mm O.D. copper tubing (alloy UNS C12200) was bent into a serpentine shape with four legs using a 25.4 mm diameter manual pipe bender. The copper sheet and tubing were cleaned with acetone and methanol. Silver solder was used to join the pipe to the copper plate and 1.6 mm high silver solder wire (45% Ag, 30% Cu, 25% Zn) and white flux paste containing water, boric acid, and potassium fluorides (both from the Safety-Silv 45 brazing kit by Harris) was used to braze the two pieces together. Care was taken to have a substantial, unbroken silver join between the copper plate and the pipe to provide good thermal conduction and structural rigidity. The assembly was then placed in an oven and slowly heated to 770 °C. It was kept at this temperature for approximately 10 minutes, then the oven was turned off and the assembly was allowed to cool naturally inside the oven. This assembly will be called the back-plate.

3.1.2 Chemical Polishing

Since the thermal process described above was performed in air, the back-plate was covered in thick layers of oxide, commonly known as scale. This scale was removed through sandblasting in preparation for chemical polishing. The chemical polishing

process was developed by Hubbard-Hall and consisted of a series of agitated chemical baths. The process is as follows: 1) agitated bath in Aquaease SL-80 (10% by volume) at 60 °C for 5 minutes, followed by a cold water rinse. 2) Agitated bath in Copperbrite (50% by volume) at ambient temperature for 3 hours, followed by a cold water rinse. Finally, 3) bath in Laserguard HFP (1% by volume) at 38 °C for 2 minutes and then dried with forced air. Aquaease SL80 is a liquid heavy-duty, basic, silicated cleaner for removing heavy oils and soils; Copperbrite is an iron-based, acidic deoxidizer, and Laserguard HFP is a high-performance anti-tarnish for all copper alloys. All chemicals were obtained from Hubbard-Hall and were diluted with distilled water.

3.1.3 Absorber Coating

After polishing, the absorber coating was adhered to the back-plate. The absorber coating is commercially available under the name TiNOX energy Cu from Almeco Solar. It has a solar absorptivity of $\alpha_{sol} \sim 95\%$ for the incident solar radiation and thermal emissivity $\varepsilon_{IR} \sim 4\%$ at 100 °C. The coating was deposited on a 0.2 mm copper backing, which was in turn adhered to the back-plate by high-performance silver paste from PELCO. This adhesive consists of a dispersion of 20 μm silver flakes in an inorganic silicate aqueous solution and has a thermal conductivity k of 9.1 W/(m·K) when dried. A thin layer of the adhesive was applied to the back-plate, the coating was placed on top, and then the whole assembly was inverted and placed under pressure. The assembly was then allowed to air dry under a weight equivalent to 20 kPa for at least 48 hours.

Finally, the adhesive was cured at 220 °C in a low-pressure nitrogen environment for at least 12 hours. The finished collector can be seen in Figure 6.

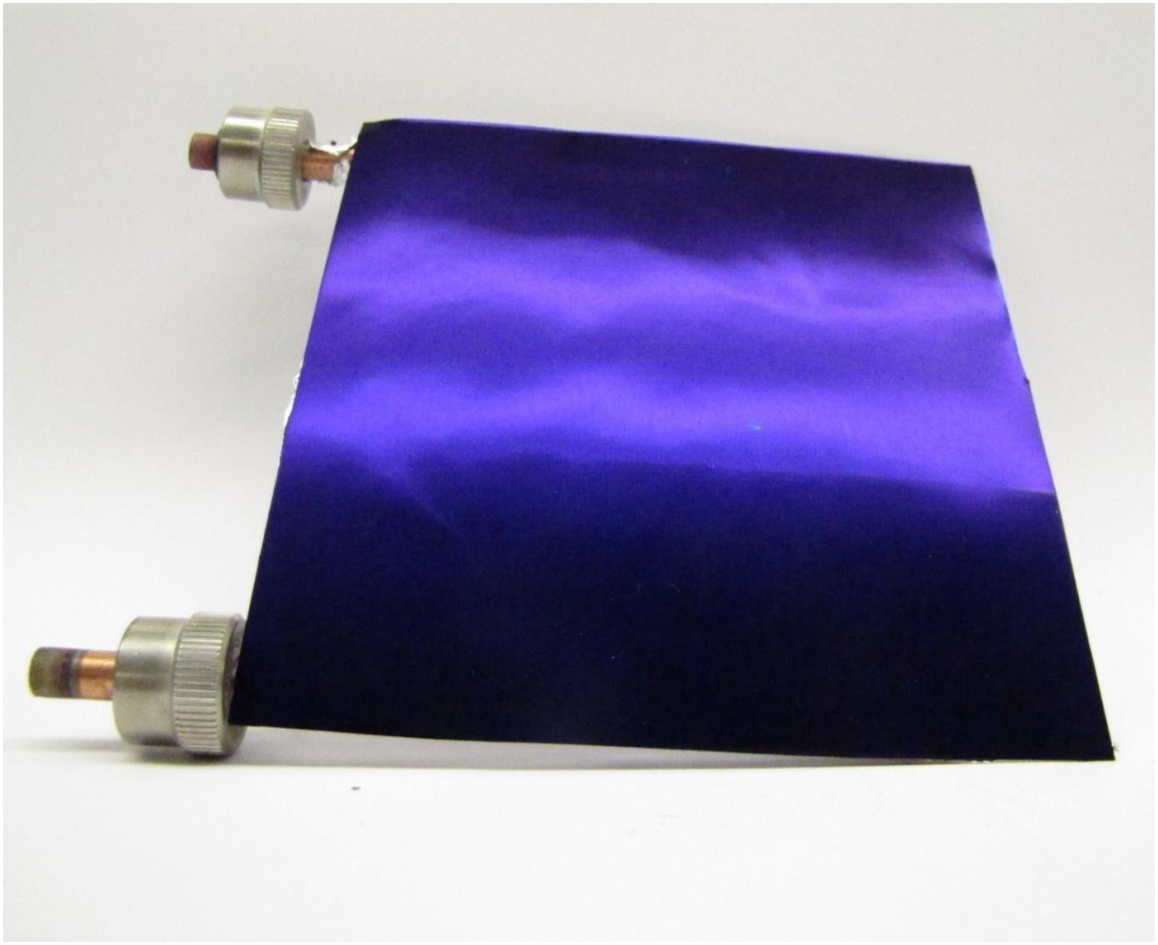

Figure 6: A photo of the Solar Collector with the selectively absorptive TiNOX coating.

3.1.4 Additional Improvements

To reduce radiative losses from the non-collecting sides of the collector, aluminum foil was adhered to the collector pipe using the above-mentioned silver paste. The foil was stretched taut between the pipes with the reflective side facing out.

Fine grade 434 stainless steel wool (average fiber diameter 50 μm) from Lustersheen was packed into the entrance of the collector creating a porous media (void fraction $\phi \sim 90\%$) that improved heat conduction from the tube wall and increased the contact area with the working fluid. Most importantly, however, the porous medium improved the boiling behavior of the liquid phase. The porous medium upset the meniscus-like boundary between the liquid and vapor, thereby creating a stable transition from liquid to vapor phase. Previous to the addition of the porous medium, violent boiling occurred at the liquid-gas boundary, causing liquid to be propelled forward through the tube. This sputtering effect reduced collector temperatures and created periodic noise in all temperature measurements.

3.2 Methanol-Steam Reformer Catalyst: Preparation and Characterization

$CuO/ZnO/Al_2O_3$ nanoparticles were synthesized in a one-step flame spray synthesis [71, 72]. Copper 2-ethylhexanoate, zinc 2-ethylhexanoate, and aluminum 2-ethylhexanoate were mixed as liquid precursors, resulting in a metal-oxide mass ratio $CuO/ZnO/Al_2O_3$ of 40:40:20. The precursor was diluted with xylene to a total metal concentration of 0.8 mol/L, similar to the method described before [73]. The diluted precursor was fed through a capillary using a gear-ring pump and dispersed by oxygen at the tip of the capillary, following ignition by a methane/oxygen supporting flame. A concentric oxygen sheath flow stabilized the burning spray in the flame synthesis reactor. The particles formed in the flame were collected with a glass fiber filter placed

above the flame. Fabrication of the nanoparticles was performed at Nanograde, Inc. (Zurich, Switzerland).

Scanning electron micrographs (SEM) were taken with an FEI XL30 SEM-FEG (300,000x, 30 kV, resolution 2-3 nm), and transmission electron micrographs (TEM) with an FEI Tecnai G2 Twin (700,000x, 200 kV, point resolution 0.3 nm). The flame spray pyrolysis (FSP) catalyst particles agglomerated in 5-15 μm pieces (Fig. 7). Further magnification on TEM showed that the individual FSP catalyst particles were approximately 20-30 nm (Fig. 7).

BET analysis was performed to determine the BET surface areas of the individual catalyst samples with a Beckman Coulter SA3100 device. An outgas temperature of 120 °C was used, and pure nitrogen was used as adsorbate gas. The experiments demonstrated that the FSP catalyst has a BET surface area of 66 m^2/g. Catalyst samples were analyzed by a Panalytical X'Pert PRO MRD HR X-Ray Diffraction System and compared with the ICDD Powder Diffraction File database. Further characterization and catalytic testing of the FSP catalyst in a conventional electrical furnace have been presented in a recently submitted publication [74].

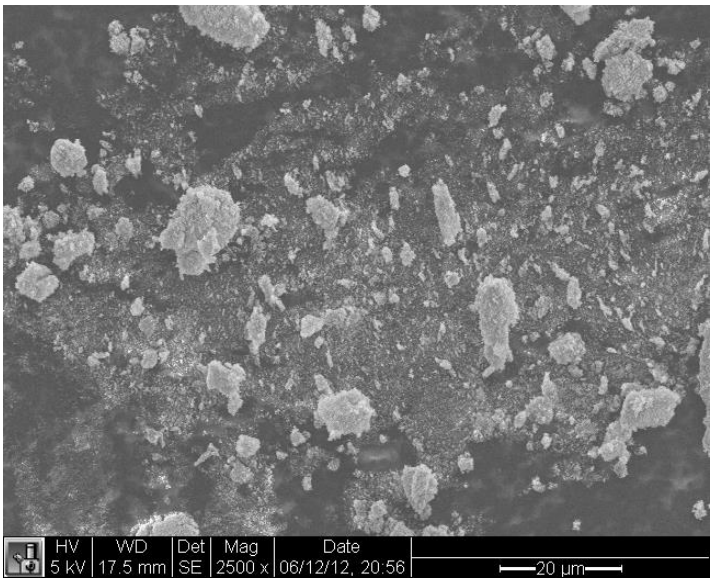

(a)

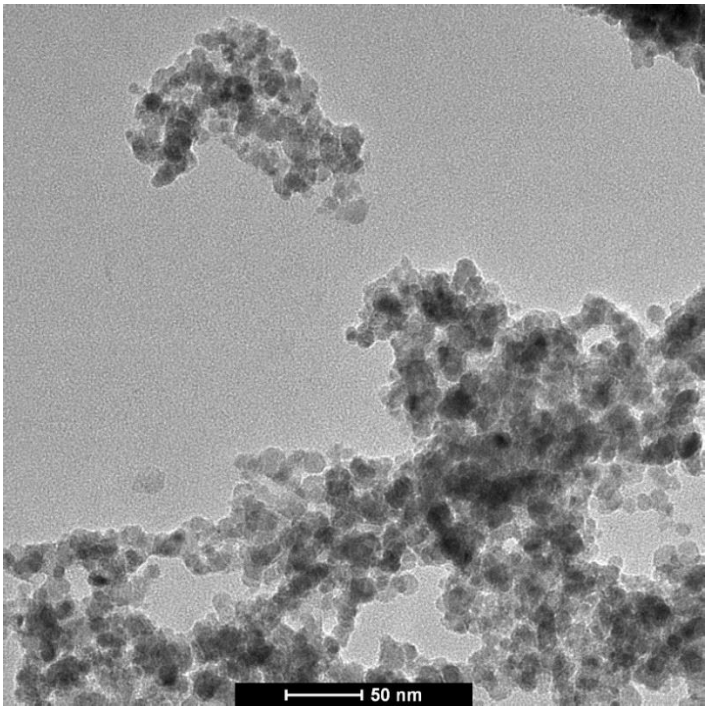

(b)

Figure 7: FSP catalyst agglomerations (5-15 µm) imaged by SEM (a), and discrete particles (20-30 nm) imaged by TEM (b) under 100,000x magnification.

3.3 Vacuum System

The vacuum system (Fig. 8) consisted of a Pfeiffer HiPace 80 Turbomolecular pump, backed by an Oerlikon Lybold D4B rotary vane pump. An ion gauge and a Pirani gauge, both from Kurt J Lesker, were used to measure the pressure in the vacuum chamber and the fore line, respectively. The chamber itself consisted of a 15.25 cm diameter 7052 glass dome with kovar seal to a 304 stainless steel ring. The bulkhead was sealed using an ISO 120 O-ring and 8 ISO C-clamps. The internal volume of the chamber was ~5 liters. The bulkhead had one evacuation port and two 6 mm feedthroughs.

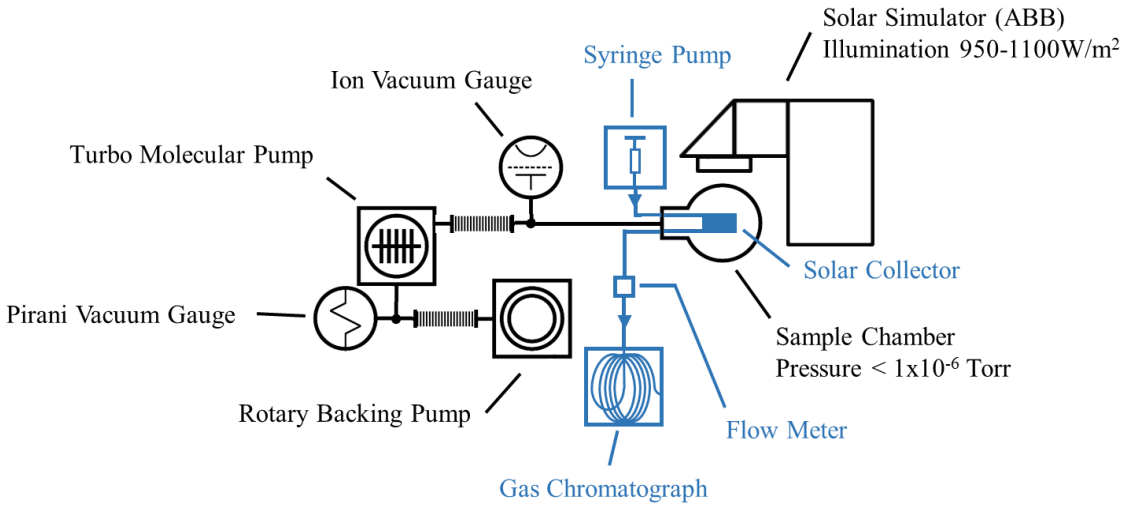

Figure 8: Schematic of the solar collector testing and vacuum system

The interior ends of the feedthroughs were connected to the collector tube with Ultra-Torr fittings. The standard O-rings were replaced with heat and chemically resistant Parofluor Ultra O-rings (FF580-75) size 2-010. Other common O-ring materials were unable to cope with the intense heat and chemical exposure of the system.

3.4 PROX Catalyst: Preparation and Characterization

Details on the preparation and characterization of the Au/α-Fe_2O_3 catalyst has been published previously and can be found in Shodiya et. al [3].

3.5 Fuel Cell and Gas Humidification Systems

The voltage and resulting current output of the PEM fuel cell were measured using a 2420 Keithley Source Meter (0.015-0.06% accuracy, <±0.4% compliance accuracy). The source meter was used to generate a voltage sweep from 0.93 V to 0.1 V across 21 data points with a 1000 ms measurement time at each point. The computer program LabTracer was used to manage the source meter. The data was then used to generate current-voltage (I-V) curves and determine the maximum power output of the fuel cell.

The gas mixtures were simulated using gas bottles and the composition was regulated using flow controllers (Cole Parmer, laminar flow gas mass controllers). The fuel cell feed gases were humidified by two water bubblers immersed in a heated water bath. Gases were sparged through the heated water inside the bubblers and reached a dew point equal to the temperature of the heated water bath. These gases then left the bubblers and traveled through heated pipes to the fuel cell. The heated pipes ensured no water condensed out of the humidified gases. Once inside the fuel cell, a serpentine flow-field exposed the gases to the membrane electrode assembly (MEA, 5 cm^2 area). The exhaust gases then exited the cell through heated pipes to a condenser bulb where

the inlet and outlet gases were combined, and excess humidity was extracted. The dry gas was then either exhausted or fed to a 7890A Agilent gas chromatograph (GC).

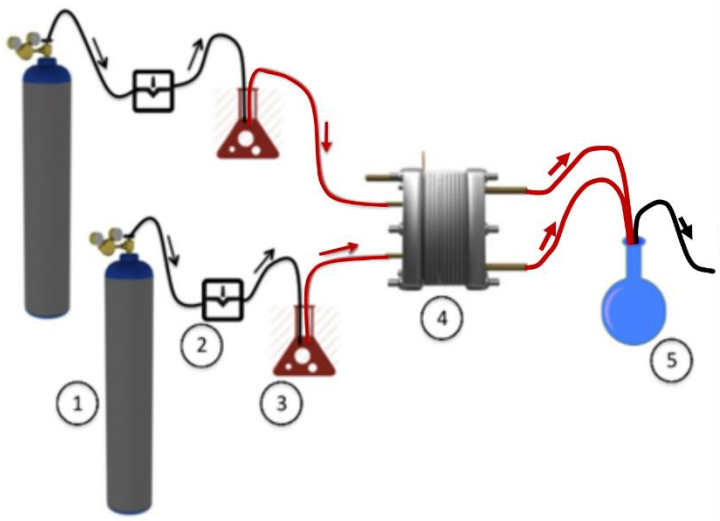

Figure 9: Fuel cell system schematic: 1. Gas bottles 2. Flow controllers 3. Heated bubblers for gas humidification 4. PEM fuel cell 5. Condenser unit.

3.6 Hybrid PROX-PEM Fuel Cell System

The hybrid PROX-PEM fuel cell system (Fig. 10) combines the PROX system described in section 3.4 with the fuel cell system of section 3.5. No flow controller was used between the PROX and the fuel cell to regulate the gas leaving the PROX. Instead, a switching valve was installed so that PROX gases could be rerouted to the GC, and pure H_2 could be fed to the fuel cell without disconnecting any section of the system. This ensured the system was always gas tight, and gas feed streams to the fuel cell were unpolluted, and controlled at all times.

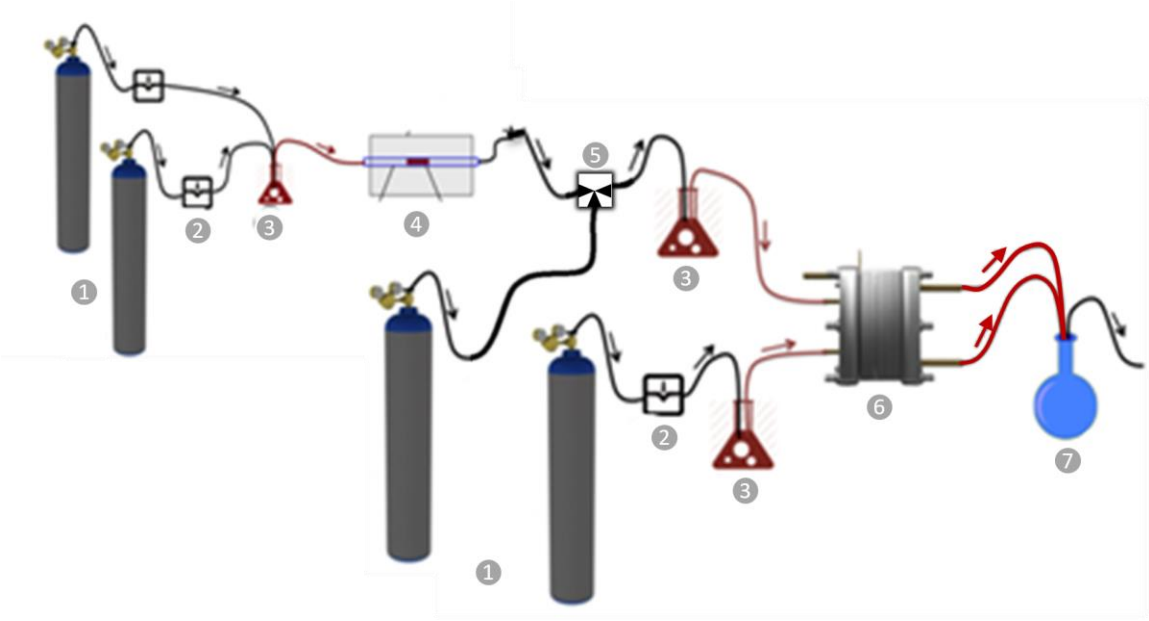

Figure 10: Combined PROX-PEM fuel cell system schematic: 1. Gas bottles 2. Flow controllers 3. Heated bubblers for gas humidification 4. PROX reactor and tube furnace 5. Three-way switching valve 6. PEM fuel cell 7. Condenser unit

4 Experimental Procedures

4.1 Universal Procedures and Equipment Pertaining to the Solar Collector

4.1.1 Solar Irradiation

Solar irradiation was simulated by a Newport Oriel Sol 1A solar simulator (ABB specification) with AM 1.5 filter and 450 W Xenon lamp. The projected circular beam had a diameter of 15 cm, with a focal length of 10 cm. The irradiance of the light was measured by a LI-COR LI-200 pyranometer (<5% error) and a Keithley 197 autoranging microvolt DMM. The nominal irradiance was determined by averaging over the entire irradiated area. The experiment was performed at ambient temperature and pressure and did not include the effects of wind or other potential outdoor conditions.

The bottom and sides of the vacuum chamber including the stainless steel ring and bulkhead were thermally insulated with fiberglass insulation wrapped in aluminum foil. Additional aluminum foil was placed to surround as much of the glass dome as possible without obscuring the collector surface. A 12 x12 cm square oculus was placed between the solar simulator and the vacuum chamber to simulate a reasonable aperture area more realistic to a commercial solar collector housing. It is important to note that the reflective foil does not serve to concentrate the incoming light onto the collector surface but rather to reflect the radiation emitted by the bottom of the hot collector and to contain the radiation that enters through the oculus. Some form of reflective coating

behind the absorber is a common insulator in high performance flat plate collectors as it reduces the effective radiative losses from non-collecting surfaces.

4.1.2 Temperature Measurements and Fuel Flow Control

Outlet fluid temperatures were measured for a variety of flow rates. Liquid inlet flow rates varied from stagnation, i.e., no flow, to 200 μl/min and were controlled by a KDS-100 syringe pump from KD Scientific (<1% error). Temperature readings were taken from HH506RA and HH147U data loggers using K-type thermocouples (KMTIN-020G, Omega) (±1.2 °C accuracy). The Inconel sheath on these thermocouples allowed accurate temperature measurements of both the water-methanol fluid and the outlet gas throughout the collector. All reported temperatures were recorded after the system had reached equilibrium defined by an outlet temperature fluctuation of <±0.5 °C/h except where noted. The reported outlet temperature for each flow rate was time averaged with a standard error of <0.01 °C. All experiments are conducted in ambient temperature of 25.8 °C (±0.8 °C).

4.2 Solar Collector Characterization

4.2.1 Control Tests and Measuring Procedures

A dummy collector was designed to test measuring techniques without the added complication of the vacuum system. The dummy collector consisted of a straight copper pipe filled with a steel wool plug, taped to a copper plate, and was placed on a VWR standard hotplate stirrer with 10 x 10 cm ceramic top. The temperature profile

under flow was recorded by pulling a type-K thermocouple through the plugged pipe. To ensure a slow, consistent, and smooth pull through the pipe, the thermocouple was attached to the pushing block of a secondary syringe pump, pulling the thermocouple at a speed of 15 μm/s. Care was taken to ensure no other parts in the system were moving.

The temperature profile within the solar collector was obtained in a similar manner. One major difference between the two systems was the direction the thermocouple was pulled. The dummy collector allowed the thermocouple to be pulled from the inlet to the outlet, while the geometry of the solar collector required the pull direction to be reversed, from the outlet to the inlet.

4.2.2 Experimental Conditions and Testing Procedures Pertaining to the Solar Collector

Outlet fluid temperatures were measured for a variety of flow rates under simulated solar irradiance of 950 - 1100 W/m^2. The vacuum chamber reached pressures below 10^{-6} Torr during testing, with a foreline pressure of ~2 mTorr.

4.3 Hydrogen Production Procedures

4.3.1 Collector and Methanol-Steam Reformer Catalyst Preparation

The catalyst nanoparticles were integrated into the solar collector in form of a packed bed: 100 or 140 mg of catalyst were mixed with 297 or 483 mg of silica sand (50 – 70 mesh, i.e. diameter of 210 – 297 μm), respectively. The larger silica particles reduce the pressure drop through the reactor compared to a packed bed consisting only of nanoparticles. The catalyst and silica particles were held between deactivated glass wool

fiber plugs inside the copper tube of the solar collector (4 mm inner and 6 mm outer diameter). The packed bed was placed close to the outlet of the solar collector, still underneath the absorber coating.

4.3.2 Experimental Procedure for Hydrogen Production

A gas flow controller (Cole Parmer) was used to supply a steady 20 ml/min standard temperature and pressure (STP) stream of N_2 to the reactor during heat-up to prevent undesirable reactions.

To test the reactor, a water-methanol mixture with a molar water-to-methanol ratio (steam molar ratio, SMR) of 1.2 using (OmniSolv HPLC Grade) methanol and biological grade water was prepared. The mixture was injected into the solar collector by a syringe pump (KDS-100, KD Scientific) with liquid inlet flow rates varied from stagnation, i.e. no flow, to 90 μl/min.

The amount of unreacted water and methanol in the product gas was limited by feeding it through an ice cooled liquid trap. Undesired condensation outside of the liquid trap was avoided by heating all tubing to above 100 °C. Control tests showed that heating of the outlet tubing did not affect temperatures within the collector. The flow rate of product gas was measured using a low-pressure gas flow meter (Cole Parmer).

Finally, the GC was used to quantify the gas composition of the product after each experimental run. The GC had a gas-sampling loop and used helium as the carrier gas. The columns used were a HP-PLOT/Q and HP-MOLESIEVE, both 30 m in length

and 0.53 mm in diameter. The HP-PLOT/Q had a 40 μm film and the HP-MOLESIEVE column 50 μm.

To maintain the reactor overnight, a low or "stand-by" liquid flow of 0.1ml/h was used. This stand-by flow ensured that undesired reactions did not occur, while limiting the degradation that could occur during long-term use.

4.4 PROX and PEM Fuel Cell Operation

4.4.1 PROX Operating Procedures

The PROX reactor contained 100 mg Au/Fe2O3 (3 wt% Au) and 300 mg silica sand (50-70 mesh). The hydrogen-rich gas consisted of 75% H_2, 24% CO_2, and 1% CO and was fed at 10 ml/min into the reactor, together with 1 ml/min synthetic air (80% N2, 20% O_2). Before reaching the PROX reactor, the gas mixture was humidified by passing through a water bath at room temperature. The PROX reactor was operated at 70 °C. The reactor temperature was maintained by a tube furnace, and was verified by a type-k thermocouple data logger.

4.4.2 PEM Fuel Cell Operation

The PEM fuel cell included a 5 cm^2 MEA from FuelCell.com (Nafion© 212 membrane, 1 mg Pt/cm^2, carbon fiber GDL). Kevlar gaskets were used to seal between the MEA and graphite plates with flow channel and the current collector plates were made of gold plated steel (all materials from FuelCell.com). The fuel cell was heated to 70 °C with external electrical heaters during operation, and gas lines were heated to

≥85 °C, where necessary to prevent condensation in the lines. For each test the system was run with an initial water bath temperature of 80 °C creating high humidity to saturate the membrane. This was done until a characteristically flooded I-V curve was observed (see Fig. 25a). The water bath temperature was then lowered to between 55 and 65 °C to begin a controlled drying process. Incrementally, the water bath temperature was increased along with the fuel cell's power output. Power measurements were typically recorded every 5 minutes, however that frequency could vary from 1 minute to 15 minutes based on the activity of the fuel cell.

4.4.3 PEM Fuel Cell Operation under CO_2 Diluted Feed Gas

During CO_2 dilution testing H_2 flow rates were unchanged. Instead CO_2 was introduced to the H_2 flow stream such that the CO_2 gas reached 10, 20, or 30% of the combined H_2-CO_2 flow rate. This was done to ensure changes in power from the fuel cell could not be attributed to an absolute decrease in the rate of active fuel entering the cell.

4.4.4 Hybrid PROX-PEM Fuel Cell Operation

Testing began by establishing a baseline of stable operation for both the PROX catalyst and the PEM fuel cell individually for a minimum of 45 minutes prior to combination. The PROX catalyst had to reduce the mole fraction of CO below 20 ppm to avoid poisoning of the fuel cell, which corresponds to a CO conversion above 99.8%. The systems were then combined using the switching valve so that pure hydrogen gas was replaced with PROX product gas. The system was then observed for between 87 and 145

minutes. After establishing prolonged stable operation of the fuel cell under PROX product gas the systems were separated, again using the switching valve, and the performance of the PROX and fuel cell were checked against the initially established baseline of stable operation.

5 Definition of Solar Collector Efficiencies

The methanol conversion η_{ref} is calculated as the molar amount of reacted methanol divided by the molar methanol inlet flow rate $\dot{n}_{in,\mathrm{CH_3OH}}$ is:

$$\eta_{ref} = 1 - \frac{\dot{n}_{out,\mathrm{CH_3OH}}}{\dot{n}_{in,\mathrm{CH_3OH}}} \quad (1)$$

where $\dot{n}_{out,\mathrm{CH_3OH}}$ is the molar amount of unreacted methanol leaving the collector. The thermal efficiency of the solar collector η_{therm} is defined as:

$$\eta_{therm} = \frac{\Delta H}{Q_{solar}}, \quad (2)$$

where ΔH is the total enthalpy rate gained by the working fluid, and $Q_{solar} = IA_{apt}$, is the solar heat input Q_{solar} equal to the product of the solar intensity, I, and the open area of the aperture, A_{apt}. Within a single phase, ΔH can be defined as $\Delta H = \dot{m}C_p(T_{coll} - T_\infty)$, where $\dot{m}$ is the fluid flow rate, C_p is the specific heat, and T_{coll} and T_∞ are the collector temperature and the ambient temperature. However, when the working fluid undergoes a phase change from liquid to vapor, the heat of vaporization must be accounted for. Thus, the full expression is

$$\Delta H = \dot{m}\left[C_{p,l}\,(T_b - T_\infty) + C_{p,v}\,(T_{coll} - T_b) + \Delta H_{vap}\right], \quad (3)$$

where $C_{p,l}$ and $C_{p,v}$ are the specific heat of the liquid and vapor phases, T_b is the boiling point of the fluid, and ΔH_{vap} is the specific heat of vaporization. The vapor–liquid equilibrium of a methanol–water binary mixture can be calculated by using the Antoine equation to compute the saturation vapor pressure. The Non-Random Two-Liquid

(NRTL) model was applied to estimate the activity coefficients and consider non-ideal mixing of the liquid phase by Renon and Prausnitz [75-77], as shown in a previous study [22]. The best fitting model for the excess enthalpy of the liquid phase was found in Horstmann et al. [78]. The specific heat capacities for liquid and vapor phase were calculated using polynomial expressions from Moran, Shapiro [79] and the DIPPR Project 801 database [80]. Based on these calculations we can were able to generate values for $\bar{h}_{vap}$ and $\bar{h}_{liq}$, and Eq. 2 simplifies to

$$\Delta H = \dot{n}_{in,total} \cdot [\bar{h}_{vap}(T_{coll}) - \bar{h}_{liq}(T_{\infty})] \quad (4)$$

where $\dot{n}_{in,total}$ is the total molar inlet flow rate, and $\bar{h}_{liq/vap}$ is the enthalpy of liquid and vapor methanol-water mixture.

Since the catalytic reaction is endothermic, the solar collector has to provide the required reaction enthalpy for the reaction to take place. The thermocatalytic efficiency $\eta_{thermocat}$ is defined as:

$$\eta_{thermocat} = \frac{Q_{use}}{Q_{solar}} \quad (5)$$

where the captured thermal energy Q_{use} consists of the enthalpy change from liquid to vapor and the reaction enthalpy of methanol steam reforming:

$$Q_{use} = \Delta H + \dot{n}_{in,\mathrm{CH_3OH}} \cdot \eta_{ref} \cdot \bar{h}_{react}\,, \quad (6)$$

where $\bar{h}_{react}$ is the reaction enthalpy.

Furthermore, it is advantageous to define an efficiency based on the useful chemical energy stored in the produced hydrogen, as defined by the lower heating value

(LHV). First, a chemical efficiency η_{chem} can be considered, comparing the LHV of the generated hydrogen with that of the methanol input:

$$\eta_{chem} = \frac{\dot{n}_{out,\mathrm{H_2}} \cdot LHV_{\mathrm{H_2}}}{\dot{n}_{in,\mathrm{CH_3OH}} \cdot LHV_{\mathrm{CH_3OH}}}, \tag{7}$$

where $\dot{n}_{out,\mathrm{H_2}}$ is the molar flow rate of produced hydrogen. The solar-to-hydrogen efficiency $\eta_{solar-\mathrm{H_2}}$ accounts for the input of solar energy:

$$\eta_{solar-\mathrm{H_2}} = \frac{\dot{n}_{out,\mathrm{H_2}} \cdot LHV_{\mathrm{H_2}}}{Q_{solar}}. \tag{8}$$

Finally, the total efficiency compares the hydrogen generation with both energy inputs:

$$\eta_{tot} = \frac{\dot{n}_{out,\mathrm{H_2}} \cdot LHV_{\mathrm{H_2}}}{Q_{solar} + \dot{n}_{in,\mathrm{CH_3OH}} \cdot LHV_{\mathrm{CH_3OH}}}. \tag{9}$$

6. Analytical Model of the Solar Collector

In order to better understand the thermodynamic properties of the solar collector, an analytical model of the collector heat transfer was developed and experimentally verified. To avoid the complexities due to developing flows close to the entrance, the analysis was limited to the thermally fully developed vapor phase. The analysis accounted for the temperature dependence of the thermal conductivity of the water-methanol vapor and the presence of the porous medium.

6.1 Thermal Conductivity of the Vapor Mixture

The thermal conductivity of the vapor mixture was calculated according to Dul'nev and Zarichnyak [81]. The thermal conductivity of the mixed gas is given as

$$k^* = k_1' \left[C^2 + \kappa(1-C)^2 + \frac{2\kappa C(1-C)}{\kappa C + (1-C)} \right], \tag{10}$$

where κ is a ratio of adjusted thermal conductivities, k_1' and k_2', of species 1 (water) and species 2 (methanol):

$$\kappa = \frac{k_2'}{k_1'}. \tag{11}$$

The quantity C depends on the volume concentration of the components and is given by the equation

$$v_2 = 2C^3 - 3C^2 + 1, \tag{12}$$

where v_2 is the volume concentration of the second component forming inclusions. Only the real and positive solution (first root) of this equation is desired. The adjusted thermal

conductivities, k_1' and k_2', are the thermal conductivities of the pure components in mixture, given by

$$k_1' = \frac{k_1}{v_1 + v_2 A_{12}'} \qquad \text{and} \qquad k_2' = \frac{k_2}{v_2 + v_1 A_{21}'}. \tag{13}$$

The coefficients A_{12}' and A_{21}' are adjustment parameters that account for the exchange of intermolecular energy and are given in the Appendix A. The values of all material properties and all calculated parameters, including the predicted thermal conductivity of the mixed gases, are given in Tables 1 and 2.

6.2 Thermal Conductivity in the Porous Medium

Nield and Bejan's work in *Convection in Porous Media* [82] was used to determine the overall thermal conductivity of the porous medium with porosity ϕ. They claim the thermal conductivity is bounded by the weighted arithmetic and harmonic means of the thermal conductivity of the fluid and steel fibers, k_f and k_s, respectively. In the following analysis, the weighted geometric mean of k_s and k_f,

$$k_G = k_s^{1-\phi} k_f^{\phi}, \tag{14}$$

was used as an estimate for the overall thermal conductivity k_G within the porous medium. The porosity ϕ was experimentally determined by measuring the mass and volume of six steel wool plugs. The mass of six copper pipes was recorded before and after the addition of the steel wool plug. The difference in mass was divided by the density of the steel, which provided the volume of the tube occupied by steel. From this, the porosity was calculated as

$$\phi = 1 - \frac{V_{steel}}{V_{plug}} = 0.903 \pm 0.0076. \quad (15)$$

6.3 Heat Transfer Model

To analytically describe the temperature profile of the vapor phase at steady-state, the flow is assumed to be thermally fully developed when leaving the boiling phase. This assumption is reasonable given that the thermal entrance length is less than 2 cm [83]. In cases where the porous medium fills a tube with internal diameter D_i, the relationship for fully developed heat transfer can be expressed as a constant Nusselt number for constant wall temperature T_W and constant wall heat flux q'', respectively [84],

$$\mathrm{Nu}_{D_i} = \frac{hD_i}{k} = 5.78 \qquad (T_w = \text{constant}) \quad (16)$$

and

$$\mathrm{Nu}_{D_i} = \frac{hD_i}{k} = 8.00 \qquad (q'' = \text{constant}). \quad (17)$$

Outside the porous medium, the Nusselt number in the pipe takes on the familiar values of 3.66 and 4.36 for constant wall temperature and constant heat flux, respectively.

The mean temperature profile $T_m(x)$ of the fluid within the pipe can be described analytically as

$$T_m(x) = T_W - (T_W - T_{in})e^{-\frac{hD_i\pi}{\dot{m}C_p}x} \quad (18)$$

in the case of a constant wall temperature, or as

$$T_m(x) = T_{in} + \frac{q''\pi D_i}{\dot{m}C_p}x \quad (19)$$

in the case of constant wall heat flux. For a constant wall heat flux, the wall heat flux can be calculated from the measured fluid temperature profile, written as

$$q'' = \frac{\Delta T_m}{\Delta x}\frac{\dot{m}C_p}{\pi D_i}, \tag{20}$$

where ΔT_m is the linear temperature difference between two points along the pipe separated by distance Δx. Using this heat flux and the convective heat transfer coefficient h calculated from the Nusselt number relations, it is possible to estimate the pipe wall temperature by

$$q" = h[T_W(x) - T_m(x)]. \tag{21}$$

The material properties used in the preceding calculations are listed in Table 1. To account for the temperature dependence of material properties, they are listed at 77 °C and 277 °C and averaged values are used for the calculations.

6.4 Energy Balance Model

The energy balance of the solar collector-reformer assembly reads:

$$Q_{use} = Q_{solar} - Q_{loss}, \tag{22}$$

where the heat losses Q_{loss} include radiative and conductive heat losses (Fig. 11a):

$$\begin{aligned} Q_{loss} = {} & Q_{loss,glass} + Q_{reflect} + Q_{emit,top} + Q_{emit,bottom} \\ & + Q_{loss,cond} + Q_{loss,other}. \end{aligned} \tag{23}$$

The reflective and absorptive heat loss by the glass of the vacuum chamber $Q_{loss,glass}$ amounts to:

$$Q_{loss,glass} = \left(1 - \tau_g\right) \cdot Q_{solar}, \tag{24}$$

with the transmissivity of the glass τ_g. The radiation reflected by the absorber plate $Q_{reflect}$ is:

$$Q_{reflect} = (1 - \alpha_{sol}) \cdot \tau_g \cdot A_{coll} \cdot I, \tag{25}$$

where α_{sol} is the absorptivity of the absorber coating in the UV-Vis-NIR range and A_{coll} is the collector area.

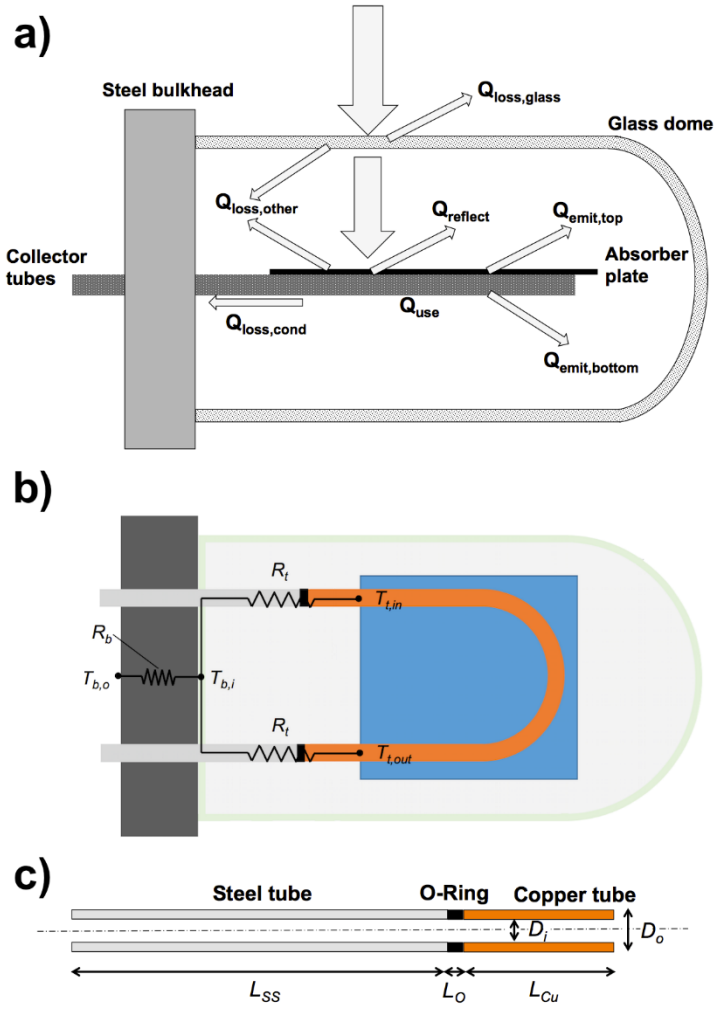

Figure 11: a) Schematic of energy balance of solar collector, b) Thermal resistor network for conductive heat transfer through tubing and bulkhead, and c) Tubing connected with O-ring.

The radiation emitted from the top-side of the absorber $Q_{emit,top}$ is approximated as:

$$Q_{emit,top} = \varepsilon_{IR} \cdot A_{coll} \cdot \sigma \cdot (T_{coll}^4 - T_g^4)\,, \tag{26}$$

with ε_{IR} as the emissivity of the absorber coating in the infrared (IR), σ the Stefan-Boltzmann constant ($= 5.67.10^{-8}\ W/(m^2 \cdot K^4)$), T_{coll} the collector temperature, and T_g the glass temperature. It is assumed that the emissivity of the glass for IR is close to 1 and the surface area of the glass dome is much larger than the solar collector. The radiation emitted from the bottom-side $Q_{emit,top}$ is identical except for the emissitivity, which is now that of a reflective aluminum coating:

$$Q_{emit,bottom} = \varepsilon_{AL} \cdot A_{coll} \cdot \sigma \cdot (T_{coll}^4 - T_g^4). \tag{27}$$

The conductive heat loss $Q_{loss,cond}$ from the solar collector through the tubing to the steel bulkhead can be modeled using a thermal resistor network analysis (Fig. 11b), taking heat conduction from the inlet region of the solar collector (T_{in}) through the inlet tubing, the outlet region of the solar collector ($T_{out} = T_{coll}$) through the outlet tubing, and the bulkhead itself into account: equation

$$Q_{loss,cond} = \frac{T_{in} + T_{out} - 2T_{b,o}}{R_t + 2R_b}, \tag{28}$$

where R_t is the thermal resistance of the tubing, R_b the thermal resistance of the bulkhead, and $T_{b,o}$ the outside temperature of the bulkhead.

The thermal resistance of the tubing is a serial network consisting of copper tubes connected to the collector, steel tubes connected to the bulkhead, and O-rings connecting these two parts (Fig. 11c):

$$R_t = \frac{\frac{L_{Cu}}{k_{Cu}} + \frac{L_O}{k_O} + \frac{L_{SS}}{k_{SS}}}{\frac{\pi}{4} \cdot (D_o^2 - D_i^2)}, \tag{29}$$

with L as the length and k the thermal conductivity of each part, D_o the outer and D_i the inner diameter. The thermal resistance of the bulkhead is calculated as:

$$R_b = \frac{L_b}{\frac{\pi}{4} \cdot k_b \cdot D_b^2}, \tag{30}$$

where D_b is the diameter of the bulkhead.

The remaining heat losses $Q_{loss,other}$ are calculated using Eqs. (22) and (23). They include all heat losses otherwise not accounted for by this simple heat transfer model, mostly attributed to the fact that the aperture is larger than the collector and some direct light misses the top-side of the collector. All material, geometric and operational properties are listed in Table 3.

7. Conceptual Model for the Practical Operation of a PEM Fuel Cell

Many models have attempted to consider in great detail the various water transfer mechanisms occurring in a PEM fuel cell [46, 48, 50, 51, 58, 63, 65, 85-88]. In current literature, there is, however, a lack of conceptual models for experimentalists active in the lab that can provide an intuition for the behavior of a fuel cell operating under a given set of conditions. This model will prioritize such a conceptual understanding needed for practical operation of a PEM fuel cell under isothermal and isobaric conditions.

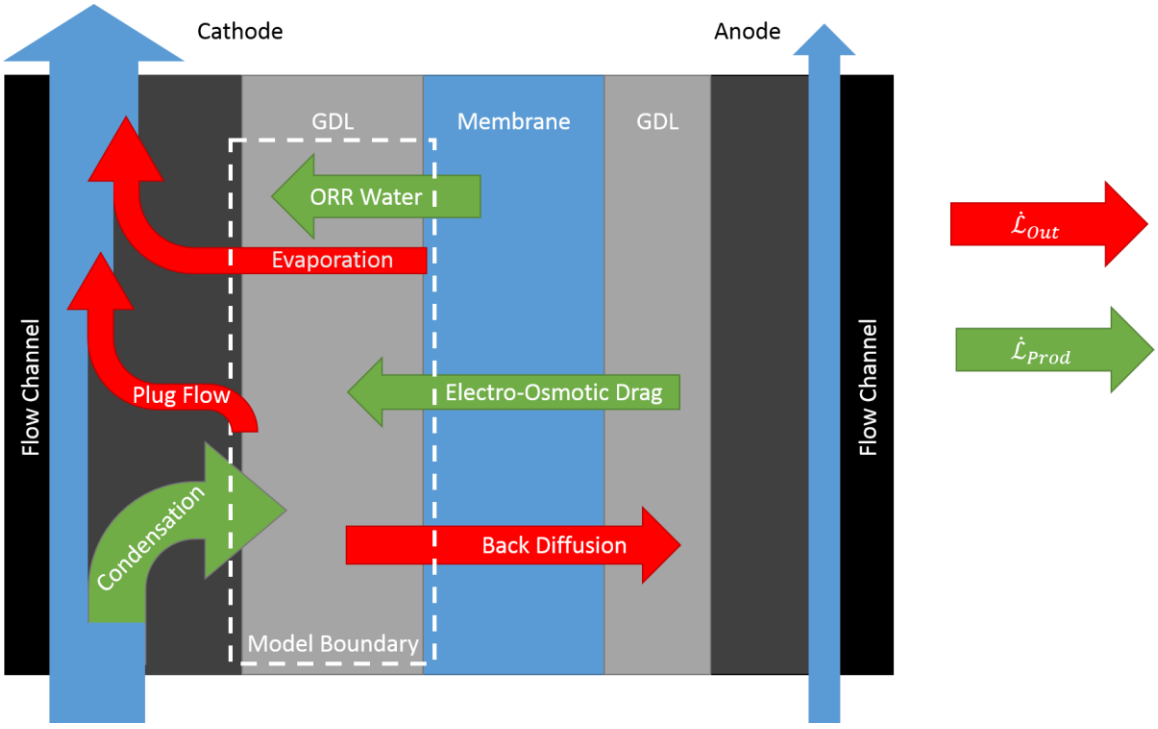

Figure 12: System schematic and definition for a conceptual model for the practical operation of a PEM fuel cell.

To begin, the model (Fig. 12) will be restricted to the cathode-side GDL, as water management on the cathode side is significantly more difficult and influential. The behavior of the fuel cell can simplistically be thought of as a balance between the five mechanisms of water transfer described earlier. This model will generalize water transfer mechanisms as either water producing, $\dot{\mathcal{L}}_{Prod}$, or water removing, $\dot{\mathcal{L}}_{Out}$, on the cathode side of the fuel cell, establishing a mass balance for water in the cathode-side GDL. Water produced from ORR, water moved from the anode to the cathode through EOD, and humidity condensed out of inlet gasses would all be sources included in $\dot{\mathcal{L}}_{Prod}$. Similarly, back diffusion, capillary flow to the flow field, plug flow in the flow field, and water removed through evaporation would all be included in $\dot{\mathcal{L}}_{Out}$.

The model assumes that when $\dot{\mathcal{L}}_{Prod} = \dot{\mathcal{L}}_{Out}$ the fuel cell will be in a steady process state. We can define a unit-less parameter

$$\eta = \frac{\dot{\mathcal{L}}_{Prod}}{\dot{\mathcal{L}}_{Out}} \tag{31}$$

, where $\eta = 1$ is a steady process state, $\eta > 1$ is a flooding process state, and $\eta < 1$ is a drying process state. The parameter η is a measure of the process state, and is distinct from the physical state of the fuel cell. It is possible to have a dry fuel cell with $\eta > 1$ and vice versa. The goal of this model is to predict future values of η given an initial physical

state (either ideal, partially flooded, or partially dried), and a starting value of the process state, η_i.

The membrane and GDL are modeled as two connected, finite reservoirs of liquid or absorbed water respectively, with capacities C_m and C_{GDL} respectively. If $\eta > 1$, unremoved water fills the membrane before filling the GDL and, likewise, if $\eta < 1$, water must be removed from the GDL before being removed from the membrane. There are two assumptions in this behavior: first, that the membrane and GDL are being affected sequentially, not simultaneously, and second, that water on the anode side is properly managed. The first assumption is done to clarify the behaviors that follow. (The accuracy of the model could be improved by introducing another unit-less parameter δ, which varies between 0 and 1 and is equal to the portion of η which goes towards filling the membrane. In essence, the presented model assumes $\delta = 1$ while the membrane can absorb water, and $\delta = 0$ whenever the membrane is fully saturated.) The assumption of a properly managed anode is supported by the prevalence of research focused on water management in the cathode [48, 58, 64, 86, 87, 89]. The model assumes that electric power production is a function of water in the membrane and GDL. Ideal operating conditions, defined as maximum power output, are achieved when the membrane is fully saturated and the GDL is empty of water. As the water content of the membrane decreases, ohmic resistance increases, and as the water content of the GDL increases, gas is blocked from reaching the catalyst layer. Either of these changes to the operating

condition decrease power output. The model assumes $\dot{\mathcal{L}}_{Prod}$ is essentially a function of power production and so behaves in a similar fashion. This assumption is supported by Owejan et al., who observed "a trend of increasing water accumulation [in the GDL] with load" from 0.1 A/cm^2 to 1.5 A/cm^2 for three different commercially available GDLs [66].

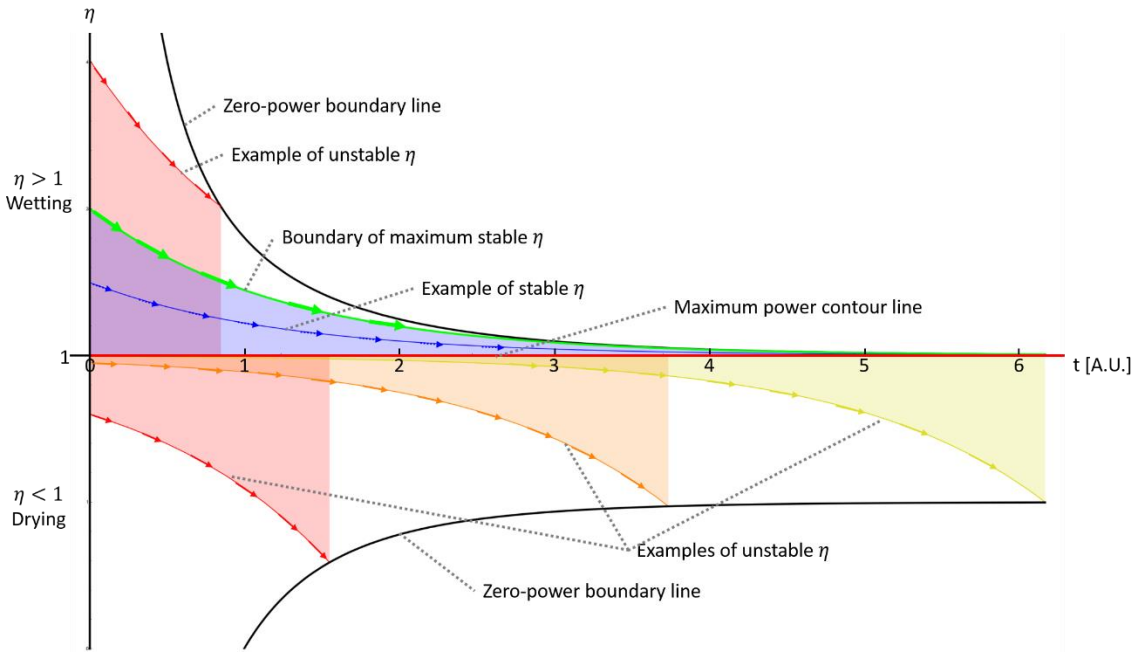

Figure 13: Characteristic curves for the behavior of a PEM fuel cell starting from an ideal physical state at $t = 0$. The red line along the x-axis represents the line of maximum power. The black lines at the top and bottom of the plot represent lines of zero-power. The blue shaded section highlights the characteristic curves for starting values of $\eta = \eta_i$ that converge to stable operation, i.e. $\eta = 1$, before reaching zero power. The green line represents the extreme edge of the blue shaded section. Other highlighted curves lead to the zero-power lines, and do not stabilize.

Based on this model, three characteristic plots of η as a function of time can be created for the three possible initial physical states, ideal, partially flooded, and partially

dried (Figs. 13, 14, and 15 respectively). The characteristic curves shown assume externally controllable variables, such as the humidity levels of the input gas and the inlet gas flow rates, remain constant. This characteristic plot is easiest to describe for an ideal initial physical state.

From an ideal initial physical state (Fig. 13), the maximum power of the system is achieved when $\eta_i = 1$, shown by the red line laying atop the x-axis. For $\eta_i < 1$, water is slowly removed from the membrane, since the GDL is already fully dry. This causes a slow but accelerating increase of ohmic resistance in the membrane and decrease of water production. At some point, t_0, the membrane is able to produce no more power. The value of t_0 for each $\eta_i < 1$ is shown by the lower black line, or zero-power line. At this point, water storage capacity of the membrane, C_m, can be defined by the integral

$$C_m = \int_0^{t_0} \dot{\mathcal{L}}_{out}(1-\eta)dt. \tag{32}$$

The value of C_m is constant for any particular membrane under isothermal and isobaric conditions.

For $\eta_i > 1$, water is being introduced to the GDL. As the GDL fills, power output and thus water production decrease. The rate of excess water production, $\dot{\mathcal{L}}_{out}(\eta - 1)$, is greatest at $t = 0$. This causes the value of η to decrease until it reaches 1, as long as there is empty volume in the GDL to accept additional water. The characteristic curve for the maximum value of η_i that will reach stability infinitesimally above zero power is shown

by the green line. For sufficiently large starting values of η_i, the GDL will be full of water and the power will be zero before η reaches 1. At the moment power reaches zero, t_0, it is possible to calculate C_{GDL}, the water capacity of the GDL, by the integral

$$C_{GDL} = \int_0^{t_0} \dot{\mathcal{L}}_{out}(\eta - 1)dt. \tag{32}$$

Like C_m, C_{GDL} is a constant for any particular GDL.

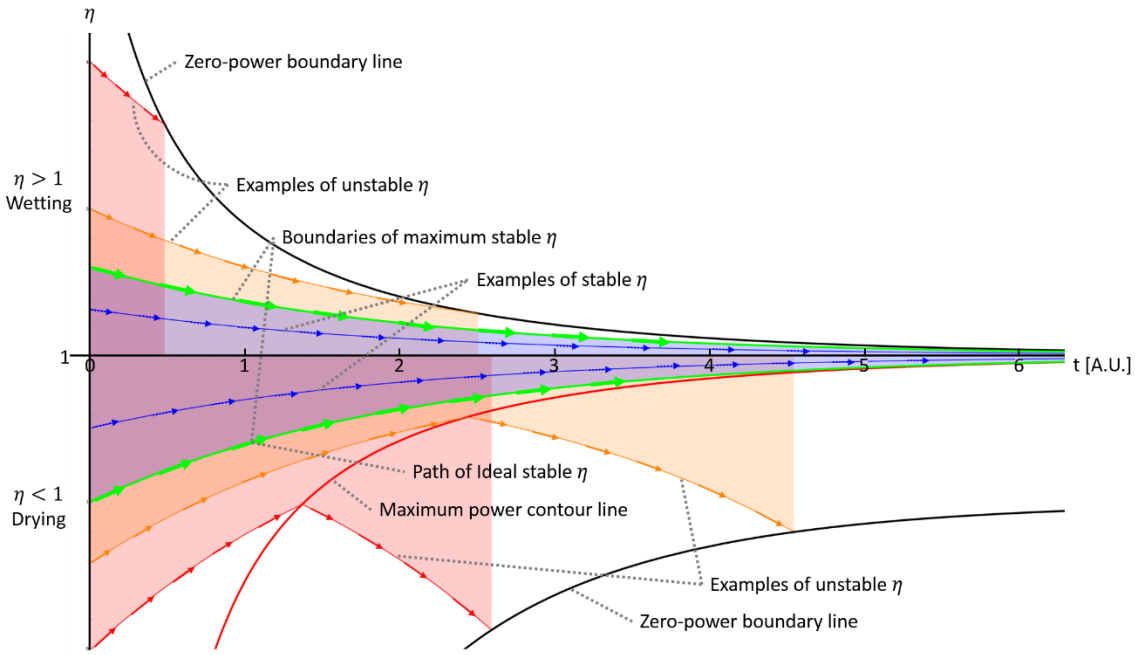

Figure 14: Characteristic curves for the behavior of a PEM fuel cell starting from a partially flooded physical state at $t = 0$. The color scheme and associated meanings are preserved from Figure 13.

Next, we can examine the fuel cell's behavior based on a partially GDL flooded initial physical state (Fig. 14). In this case, the behavior for $\eta_i > 1$ is similar to that of the ideal case, but with the characteristic curves shifted such that

$$(1 - \phi_{i,flooded})C_{GDL} = \int_0^{t_0} \dot{\mathcal{L}}_{out}(\eta - 1)dt, \tag{34}$$

where $\phi_{i,flooded}$ is the percentage of the GDL that is pre-flooded.

For $\eta_i < 1$, however, power and water production initially increase as water is removed from the GDL and more of the catalyst is exposed to reactant gas. This causes η to approach 1 as the GDL dries out. If η reaches 1 before excess water from the GDL is completely removed, the system will be stable. In this case, the equation

$$\phi_{i,flooded}\, C_{GDL} \geq \int_0^{t} \dot{\mathcal{L}}_{out}(1 - \eta)dt \tag{35}$$

holds. There exists a particular value of $\eta_i = \eta_{i,ideal}$ which will reach 1 precisely when the excess water in the GDL has been completely removed, and the membrane has not yet been affected. The characteristic curve for $\eta_{i,ideal}$ is shown by the lower green curve. For $\eta_{i,ideal}$ at $t = t_{ideal}$, the two sides of Equation (35) are equal and $\eta = 1$. At this point, the system is in the ideal physical state, and power output is maximized. For $\eta_{i,ideal} < \eta_i < 1$ the power achieved after reaching stability will be greater than the initial power but still less than the maximum possible power. Additionally, for each value of $\eta_i < \eta_{i,ideal}$ there exists some time $t = t_{max\ power} < t_{ideal}$ where the two sides of Equation (35) will be equal, but $\eta < 1$. Instantaneously, at $t = t_{max\ power}$, the system will be in the ideal state, but because η is still tending towards drying, the membrane will begin to dry out, and the curve begins to resemble the curves for $\eta < 1$ from the ideal

initial physical state. The red line below the axis in Figure 14 shows the maximum power line at $t = t_{max\ power}$ for all $\eta_i < \eta_{i,ideal}$.

Finally, we can look at behavior given a partially dried initial physical state (Fig. 15). As before, solid black lines indicate lines of zero-power, while the solid red line indicates a line of maximum power. For the drying process state, $\eta < 1$, the characteristic curves resemble those seen in the ideal initial physical state, but shifted such that

$$(1 - \phi_{i,dried})C_m = \int_0^{t_0} \dot{\mathcal{L}}_{out}(1 - \eta)dt, \tag{36}$$

where $\phi_{i,dried}$ is the percentage of the membrane that is pre-dried.

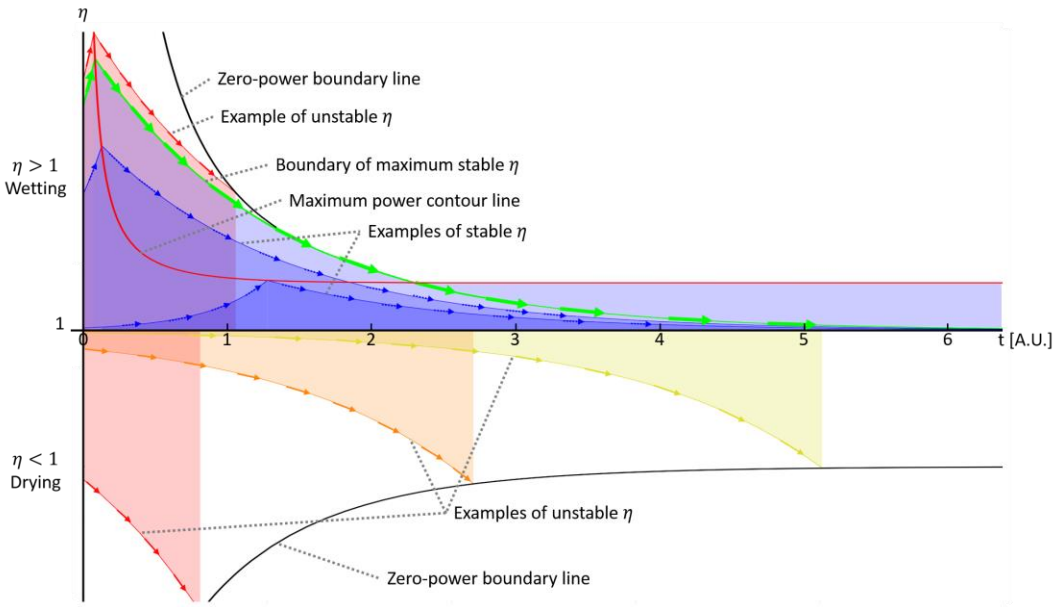

Figure 15: Characteristic curves for the behavior of a PEM fuel cell starting from a partially dried physical state at $t = 0$. The color scheme and associated meanings are preserved from Figure 13.

For $\eta_i > 1$, excess water will be absorbed by the membrane, reducing ohmic losses, and increasing water production. Thus, the model predicts an accelerating growth in η until the membrane is saturated

$$\phi_{i,dried}\, C_m = \int_0^{t_{max\ power}} \dot{\mathcal{L}}_{out}(\eta - 1)dt, \tag{37}$$

whereupon the system will briefly be in the ideal state before the excess water begins flooding the membrane. At this point, the characteristic curves match those seen in the ideal initial physical state for $\eta > 1$. The green line shows the characteristic curve for the maximum value of η_i able to reach stability. It will tangentially touch the zero-power line at some point before crossing the maximum power line. This creates an envelope of possible curves bounded by three lines, the blackline for zero-power, the green line for maximum stable η_i, and the red line for maximum power. It should be noted that the light blue section highlighted between the green and red lines for high values of t is accessible by curves beginning with η_i only slightly greater than 1. All such curves would eventually reach stability after passing through maximum power. For all these curves, maximum power is reached at the same value of η, thus they would follow the same flooding curve post maximum power. This would suggest that all of these curves would show the same loss in power compared to the ideal state, and that for a range of sufficiently small values of η_i the final stable power output is a constant.

8. Results and Discussion

8.1 Solar Collector Characterization

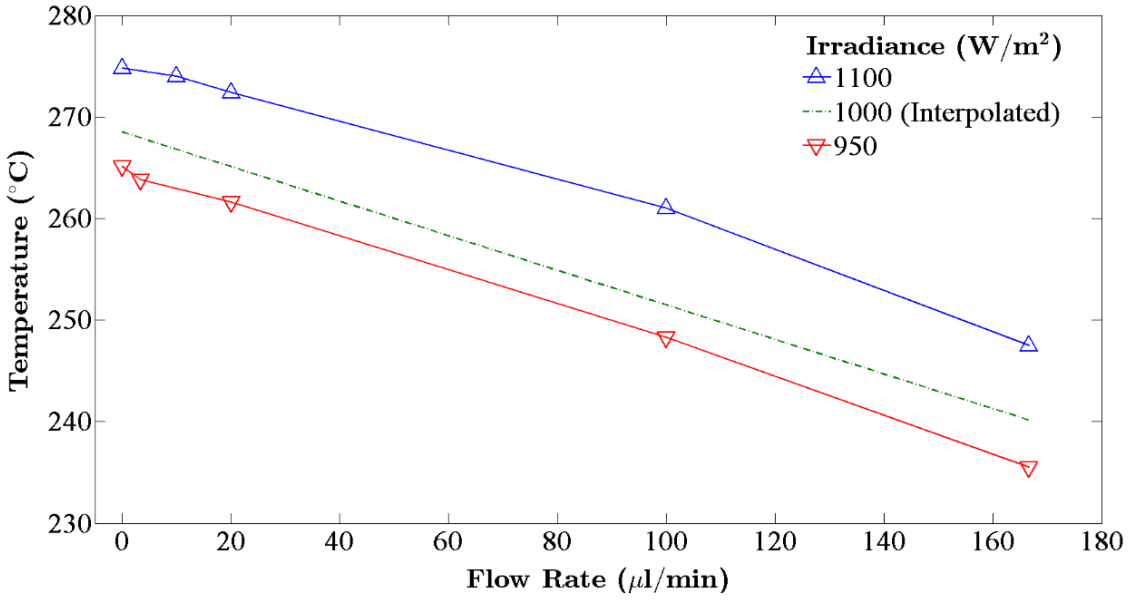

Figure 16: Exhaust gas temperature as a function of flow rate for the solar collector.

The outlet gas temperature of the solar collector exhibits a nearly linear dependency with the inlet liquid flow rate (Fig. 16). Outlet gases reached 275 and 265 ±1 °C at stagnation (no fluid flow), under 1100 and 950 W/m² irradiance, respectively. A 14% decrease in solar power from 1100 to 950 W/m² resulted in a reduction in outlet temperature of only 4%. Figure 16 also includes a linear interpolation between the two measured results to estimate the outlet temperatures expected for 1000 W/m² irradiance (= 1 sun), leading to a stagnation temperature of 268.5 °C. The outlet temperature of the solar collector remains high even for high flow rates. For liquid inlet flow rates up to 113 μl/min, temperatures above 250 °C were obtained, which is

equivalent to 0.68 l/h per m² of irradiated area. Over the two orders of magnitude tested, outlet temperatures decreased just 0.17 °C per µl/min. At this rate, temperatures above 150 °C could be achieved for liquid inlet flow rates up to 760 µl/min or 4.56 l/h per m² of irradiated area.

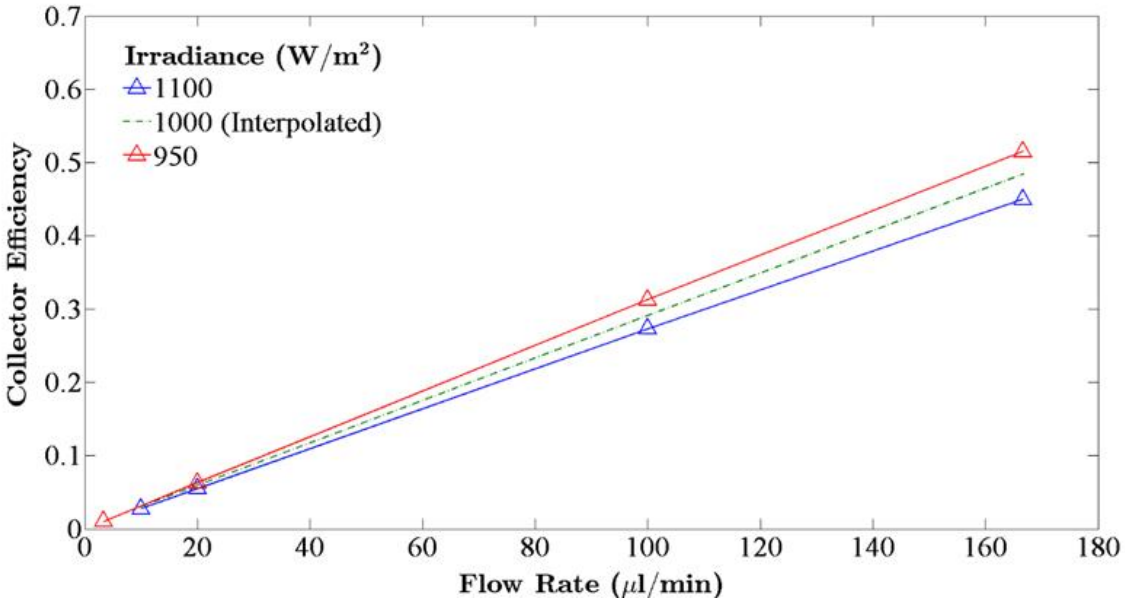

Figure 17: Collector efficiency as a function of flow rate for the solar collector.

Like outlet temperature, the collector efficiency showed a linear, though increasing trend with liquid inlet flow rate (Fig. 17). Efficiencies greater than 45% were achievable for flow rates above 166 µl/min (equivalent to 1 l/h per m² of irradiated area) and at temperatures up to 247 °C. Previous collector designs discussed in scientific literature have operational temperatures at least 70 °C cooler at comparable efficiencies [19]. Simultaneously, at the authors' target operational temperature of 250 °C, efficiencies up to 28.1% could be attained at 950 W/m² solar irradiance and 41.7% for

1100 W/m^2. The strictly linear behavior of the solar collector efficiency indicates that there was no change in the heat transfer mechanism across the range of tested flow rates; obviously, for higher flow rates the efficiency of the system will eventually not increase linearly anymore. For the highest flow rate tested in this study, 166.7 μl/min, an interpolated collector efficiency of 49% was achieved at 239.5 °C and 1000 W/m^2 solar irradiance.

Figure 18 shows the temperature profiles of the water-methanol mixture within the dummy collector heated by a hotplate. By manually changing the nominal temperature of the hotplate, the outside wall temperature of the collector was varied. Inset below the graph is a schematic of the dummy collector to scale aligned with the temperature profiles. Two notable disturbances around 60 and 80 mm were caused by physical transitions within the dummy collector. The first disturbance at 60 mm was caused by the transition from the copper pipe to the Ultra-Torr fitting and this transition is also accompanied by a discontinuity in the porous medium, where two steel wool plugs abut each other. The drop in temperature at approximately 80 mm, most noticeable for the lowest wall temperature, corresponded with the location of the Ultra-Torr O-ring, which apparently compromises the heat transfer locally. Aside from these explainable and slight deviations the temperature profiles of all tests matched excellently with the analytical model for constant wall temperature. The difference between the wall and fluid temperatures decreased exponentially. After 110 mm, the

fluid temperatures reached values close to the wall temperature (shown on the right side of Fig. 18). The analytical model (shown as solid lines with larger symbols) described the temperature profiles with a 1% error compared to experimental data (shown as dotted lines) collected for all cases in the dummy collector.

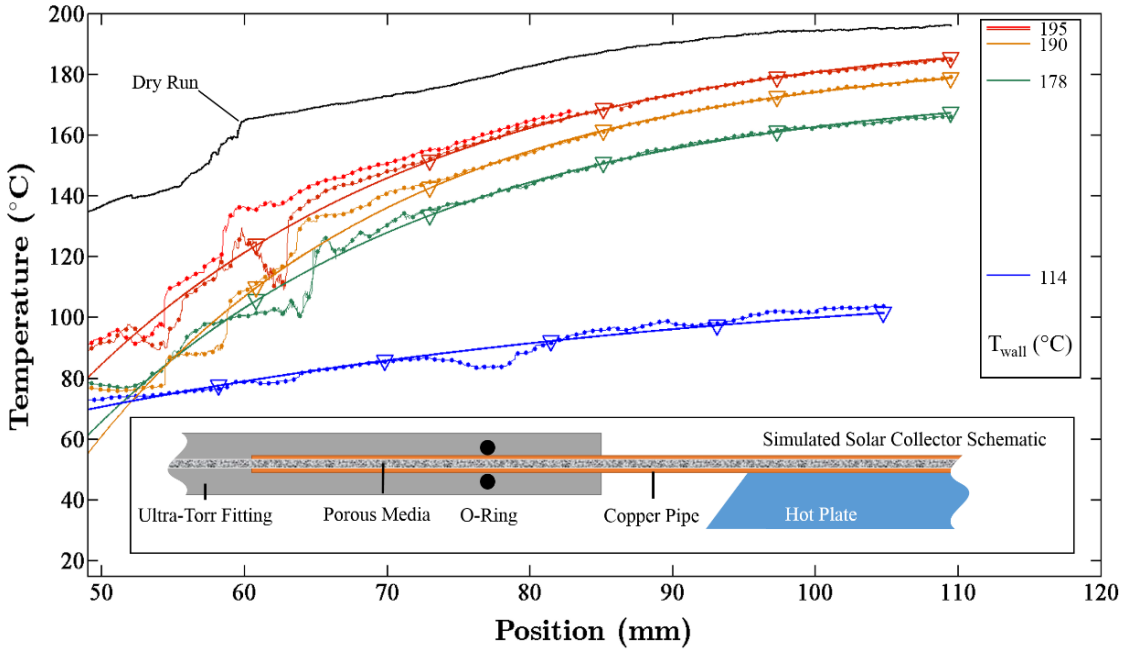

Figure 18: Temperature profiles inside dummy collector on a hotplate for different wall temperatures.

By contrast, the temperature profiles of fluid within the actual solar collector were dominated by sections of a linear profile, corresponding to a constant heat flux condition. Looking at Figure 19, there were four clear sections marked by changes in slope of both the dry run profile (no fluid flow, only ambient air in the pipe) and the fluid flow runs. These sections can be attributed to physical changes in the collector, shown by the schematic insert to scale. Before 38 mm (section I), the fluid was passing

through the porous medium. From 38 to 56 mm (section II), flow occurred in the open pipe. From 56 to 65 mm (section III), the temperature increased dramatically and after 65 mm (section IV), the temperature increased linearly as in section II. The transition from section I to II clearly corresponded to the transition from the porous medium to the open pipe. Section III was possibly due to an inhomogeneity in the collector. Section IV indicated a return to the heat transfer seen in section II.

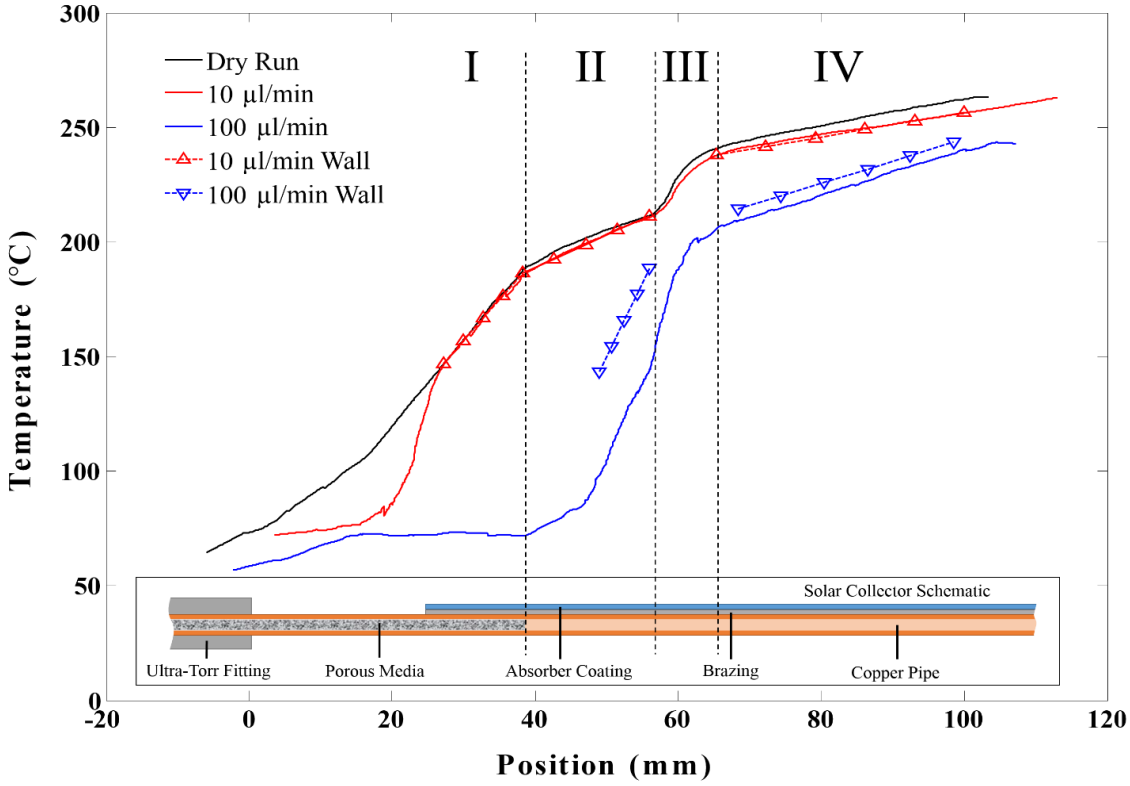

Figure 19: Temperature profiles of fluid inside the solar collector at 1100 W/m² illumination for two different flow rates and dry run. Wall temperatures were calculated assuming constant heat flux.

Using the constant heat flux boundary condition, it was possible to estimate the wall temperature profile of the solar collector, shown in Figure 19 by the dashed lines.

Wall temperature estimates for the 10 and 100 μl/min flow rates never exceeded the dry wall temperature profile, and closely followed the experimental fluid temperature profiles. The difference in temperature between wall and fluid for the 10 μl/min flow rate was very small (<1 °C), as would be expected. At higher flow rates, the difference between the wall and fluid temperatures was significant. In section II, the calculated temperature difference between wall and fluid at a flow rate of 100 μl/min was 45 °C and decreased to 5 °C in section IV.

Figure 19 demonstrates that the heat transfer between the water-methanol mixture and the solar collector is very efficient. While the final fluid outlet temperatures for 10 μl/min and 100 μl/min are 274 °C and 261 °C, a fluid temperature of 262.6 °C for 10 μl/min and 242.8 °C for 100 μl/min was achieved before the end of the first leg of the serpentine collector (approximately 110 mm in the figure). Additionally, the phase change region at 76.8 °C can be clearly seen for both flow rates. For 100 μl/min, approximately 20 mm of tube length were required to provide sufficient evaporation heat.

The data attained from the dummy collector shows that the nature of using the sun as a heat source through solar absorption is fundamentally different from a hot plate or other heat source capable of maintaining a specific temperature through the provision of power on demand. The dummy collector behaved very closely to a constant wall temperature case after the transition to the copper pipe. This is obvious from the

exponential decrease in temperature difference between the collector wall and the fluid, as seen for all flow rates in Figure 18. The high thermal conductivity of the copper ensured that the dummy collector tube was very close to isothermal, even in the entrance region without direct contact with the hotplate. This is distinctly different from the solar collector, which is limited by the absorption of incident radiation. In the case of solar power with limited area-wise density, the enthalpy change of the fluid consumed large parts of the provided heat, before it could dissipate through the copper collector. Thus, the profile of the fluid temperature in the solar collector was determined by a constant heat flux condition instead of the constant wall temperature condition.

8.2 Hydrogen Production

For the 100 mg reactor, experiments are performed in increments of 1 mL/(min·m^2); 1 and 2 mL/(min·m^2) are measured on day one, and 3 – 6 mL/(min·m^2) are measured on day two. Likewise, the 140 mg reactor is tested in increments of 1 mL/(min·m^2), with 3 – 5 mL/(min·m^2) measured on day one, and 6 – 9 mL/(min·m^2) measured on day two.

The temperature of product gas at the end of the collector shows an approximately linear, decreasing trend with inlet flow rate, see Figure 20a. This is in agreement with findings from a previous study of a similar collector without catalyst loading [27]. The collector temperature is above 235°C for all measurements, indicating sufficiently high reactor temperature for methanol steam reforming. The temperature

difference between the two reactors over similar flow rates increases from 4.1°C at 3 mL/(min·m^2), to 5.6°C at 6 mL/(min·m^2). Under a stand-by liquid flow rate of 0.167 mL/(min·m^2), temperatures stabilize overnight to 263.7 and 259.7°C for the 100 and 140 mg reactors, respectively.

The observed temperature decrease from the 100 mg to the 140 mg reactor is most likely the result of two factors independent of the reactor itself: decreased solar illumination and degraded structural integrity of the solar collector. The collector was subjected to over 30 days of active testing and was dismounted from the vacuum chamber at least ten times. This excessive dismounting and reassembling led to some deterioration of the bond between the absorber coating and the copper back-plate, which is essential in transferring the absorbed solar heat to the rest of the collector and is likely to be blamed for the slightly decreased temperatures seen in the 140 mg reactor tests.

Complete conversion is achieved up to flow rates of 3 and 4 mL/(min·m^2) for the 100 and 140 mg reactors, respectively, as shown in Figure 20b. The methanol conversion of the 100 mg reactor decreases from 100% to 58.5% between 3 and 6 mL/(min·m^2). The methanol conversion of the 140 mg reactor decreases from complete conversion to 59.7% between 4 and 9 mL/(min·m^2). The methanol conversion decreases with inlet flow rates due to a lower reactor temperature (as shown in Fig. 20a) and a reduced residence time. Still, liquid inlet flow rates up to 5 mL/(min·m^2) result in almost complete methanol conversion for the larger reactor.

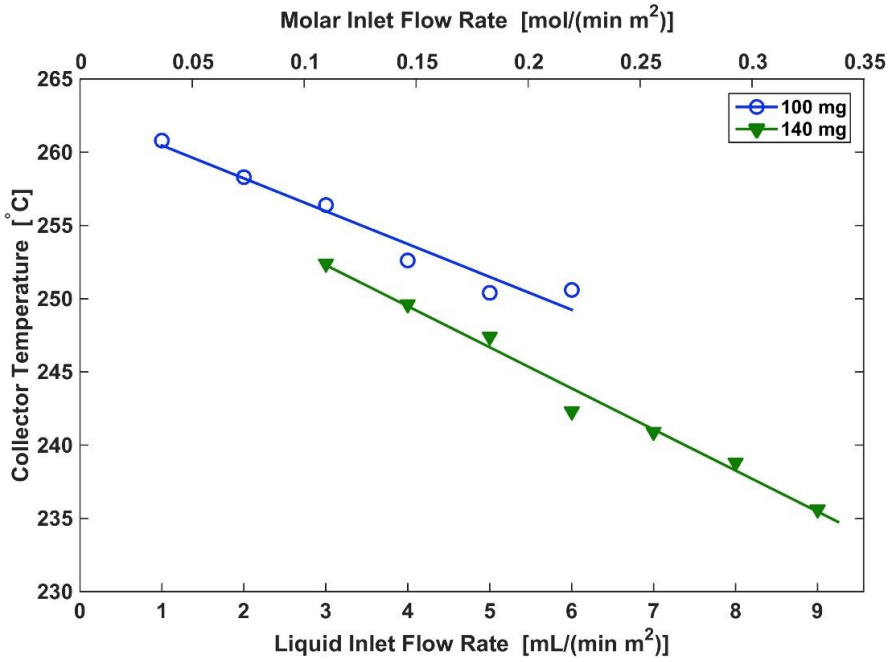

(a)

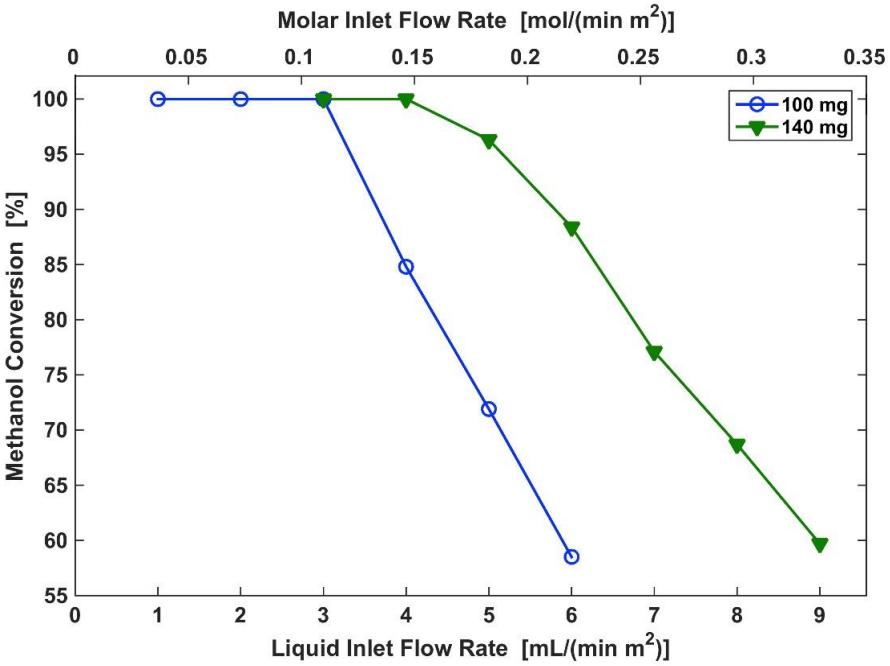

(b)

Figure 20: (a) Collector temperature as the temperature of the reformate gas as a function of liquid inlet flow rate. (b) Methanol conversion as a function of liquid inlet flow rate.

As demonstrated in Figure 21, the hydrogen flow rates of the 100 and 140 mg reactors reach maxima of 4.49 and 6.62 $L_{STP}/(min \cdot m^2)$ at liquid flow rates of 5 and 8 $mL/(min \cdot m^2)$, respectively, which corresponds to hydrogen production of 739 and 1088 W/m^2, respectively, considering the LHV of hydrogen. The hydrogen production shows flat maxima for both reactor sizes. As more liquid fuel is provided to the reactor, the methanol conversion decreases, until finally the reactor reaches the peak of hydrogen production. Simultaneously, increased liquid flow rates continue to decrease the temperature of the collector, which reduces the reaction rate of the catalyst, and thus reduces the overall hydrogen gas flow rate.

The composition of the product gas is very stable and hardly changes with flow rate and temperature, except for CO, as expected for methanol steam reforming at the relevant temperature: The molar composition of the reformate mixture is 75.0% H_2 (standard deviation: 1.1%) and 24.6% CO_2 (standard deviation: 0.34%) for all tests. With higher inlet flow rate and consequently lower reaction temperature, the amount of toxic CO by-product decreases, from 1.5% for the lowest flow rate to 0.2% for the larger reactor and the highest flow rate. Especially when used in combination with a low-temperature PEM fuel cell, the removal or oxidation of CO is a critical challenge [37] and lower CO generation in the fuel reformer lessens this burden. For the conditions achieving highest efficiencies in this study, the CO mole fraction is typically between 0.2 and 0.3%.

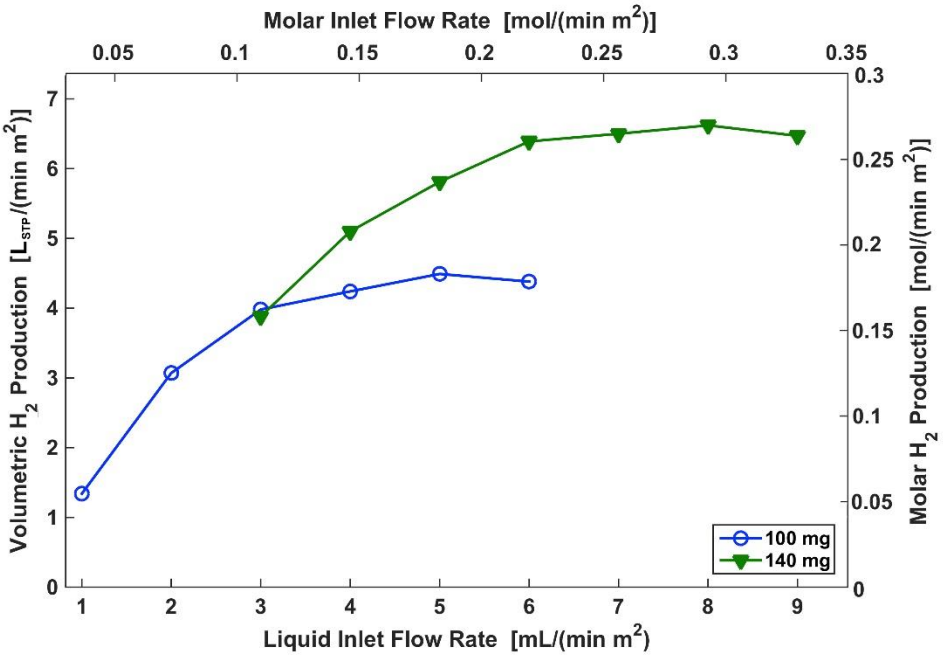

Figure 21: Hydrogen production rate per collector area as a function of liquid inlet flow rate.

The thermal and thermocatalytic efficiencies of both reactors are shown in Figure 22a. The thermal efficiency increases linearly with inlet flow rate for both reactors, from 2.0% to 12.2% for 1 to 6 mL/(min·m²) and 100 mg catalyst, and from 6.4% to 18.8% for 3 to 9 mL/(min·m²) and 140 mg catalyst. Due to the increased methanol conversion for the larger reactor size, the thermocatalytic efficiency is slightly higher for 140 mg compared to 100 mg at 3 – 6 mL/(min·m²). The highest efficiency is reached at the maximum flow rate of 9 mL/(min·m²) for 140 mg catalyst, amounting to 24.1%. This indicates that nearly one quarter of the incoming sunlight is captured and used to pre-heat, evaporate, and react the water-methanol mixture.

The chemical, solar-to-hydrogen, and total efficiencies are shown for both reactors in Figure 22b. The chemical efficiency comparing the LHV of generated hydrogen with the input methanol achieves approximately 120% for low flow rates, corresponding to full methanol conversion. For higher flow rates, the chemical efficiency decreases with decreasing methanol conversion. Since the solar energy input is constant for each reactor (with a small difference between the two reactors), the solar-to-hydrogen efficiency follows the result of hydrogen production. For 100 mg catalyst, the maximum solar-to-hydrogen efficiency amounts to 50.3% at 5 mL/(min·m^2); for 140 mg, the maximum is 77.6% at 8 mL/(min·m^2). In other words, more than three quarters of the solar energy is converted to hydrogen. The total efficiency, taking both the input of sunlight and methanol fuel into account, reaches a flat maximum of 33% for the smaller reactor for inlet flow rates of 3 – 6 mL/(min·m^2). For the larger reactor, this maximum efficiency is 43% at 5 – 7 mL/(min·m^2).

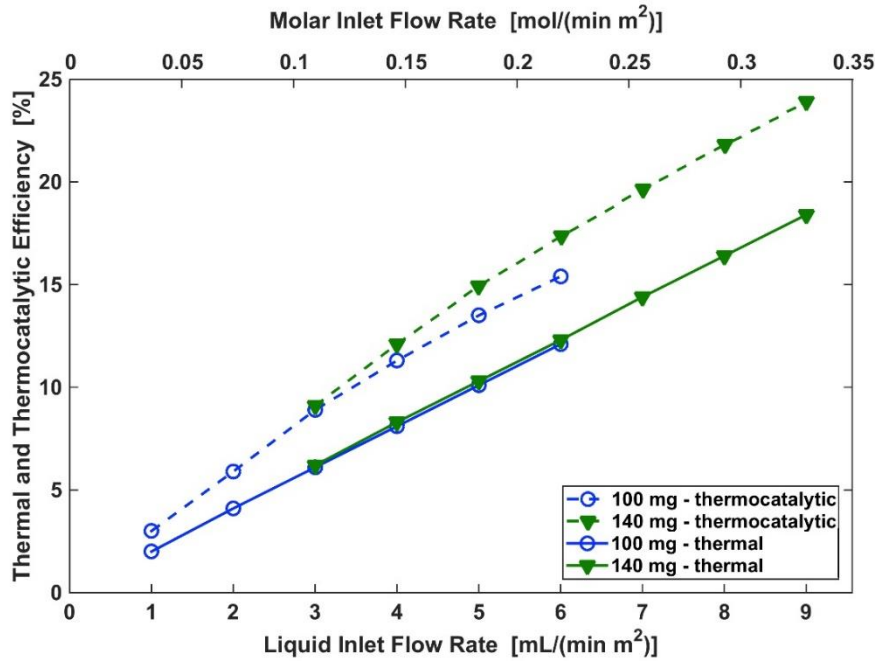

(a)

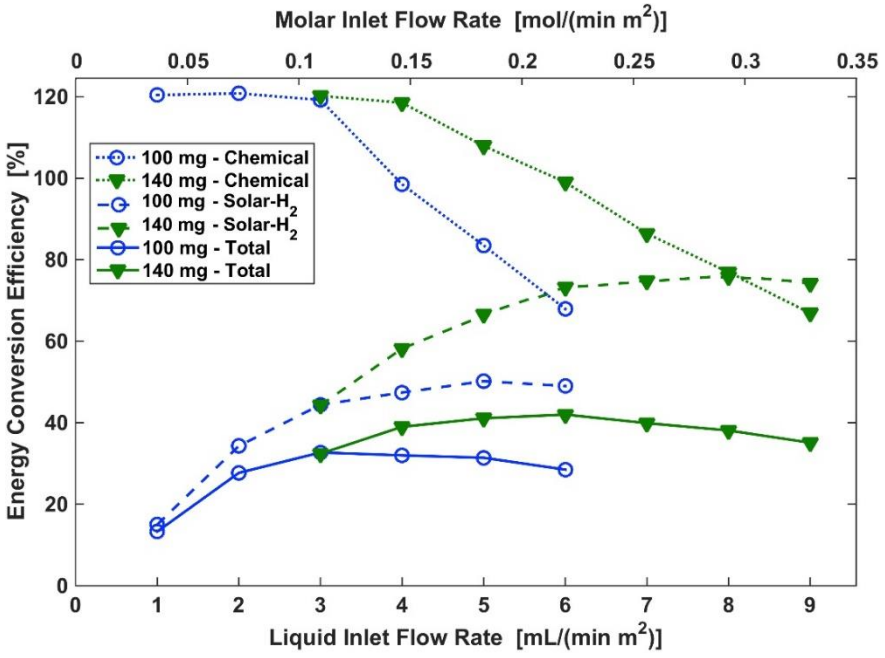

(b)

Figure 22: (a) Thermal and thermocatalytic efficiency as a function of liquid inlet flow rate. (b) Chemical, solar-to-hydrogen, and total efficiency as a function of liquid inlet flow rate.

8.3 Heat Transfer Analysis

Figure 23 shows the captured thermal energy Q_{use} and different heat losses for the solar collector containing 140 mg catalyst. $Q_{loss,glass}$, $Q_{reflect}$, $Q_{emit,top}$, $Q_{emit,bottom}$, and $Q_{loss,cond}$ change only slightly with different inlet flow rate. Q_{use} increases with flow rate, mostly due to the increase of required heating for the phase change of the inlet flow. Q_{solar} amounts to 14.0 W in this case, equivalent to the sum of all heat transfer elements shown in Figure 23.

The heat losses due to emission from the top-side of the collector $Q_{emit,top}$ represent the largest heat loss (~25% of the solar input), followed by emission from the bottom-side $Q_{emit,bottom}$ (~20%). This demonstrates the essential importance of using materials with low emissivity in the IR. While the TiNOX selective absorber coating of the solar collector is an excellent material, its emissivity at relatively high temperatures of approximately 250°C could be further improved. The bottom-side of the solar collector is far from ideal: It was covered with aluminum foil to increase its reflectivity, but a high-quality reflective coating applied directly onto the collector structure would have significantly reduced these losses. Using optimized coatings on both sides has high potential to improve the performance of the collector, since emission from both sides accounts for 45% of the heat losses of the described collector.

Heat losses due to conduction through the tubing and to absorption of light by the glass container account for another 15% of the total heat losses. Using a glass with

lower absorptivity and tube connections with lower conductivity could further improve the solar collector.

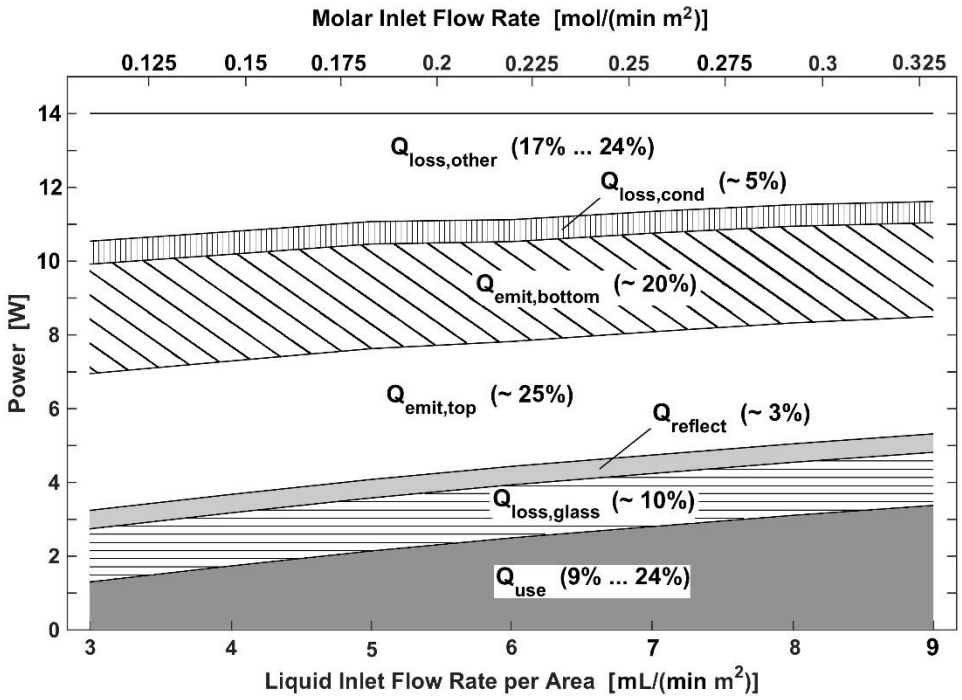

Figure 23: Energy balance of solar collector containing 140 mg catalyst for different flow rates. Numbers in parentheses show the relative contribution of all heat transfer elements.

8.4 Effect of CO_2 Dilution on Fuel Cell Performance

The performance of the fuel cell is clearly inhibited by the introduction of CO_2 into the anode feed gas compared to pure hydrogen. Figure 24 shows the recorded maximum power output of the fuel cell when operated with pure H_2, and diluted with 10%, 20%, and 30% CO_2. The grey shaded portions of the plot indicate the data used for calculating the average maximum power, which is shown by the solid horizontal lines. Raw data is shown by the dotted lines.

Table 4 gives the average maximum power, elapsed time, and aditional information about each test.

From Figure 24, there is a clear, but subtle decrease in power with increasing concentrations of CO_2. It is also clear that after exposure to CO_2 for aproximately 10 hours the fuel cell was able to recover to pre-exposure performance levels with pure H_2. This would suggest no CO_2 poisoning of the cell.

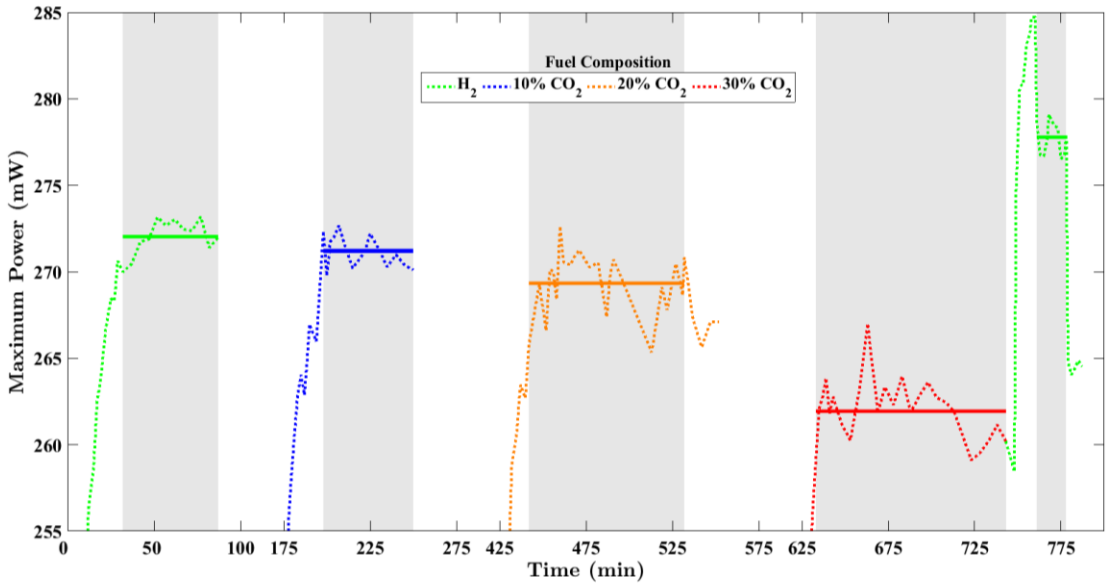

Figure 24: CO_2 dilution and its effect on PEM fuel cell performance over time.

It is important to note the time axis has three breaks in it at 100-175 minutes, 275-425 minutes, and 575-625 minutes. These portions of the data are not shown because they are sections where the fuel cell was either partially dried, or heavily flooded. The distinciton of what data what viable was based on an examination of the I-V curve. Data that was strongly linear at high current, lacking the distinctive downward curve

indicative of mass transfer limitations, was deemed dry. Data that showed markedly low power of 30-100 mW, a sharp drop in voltage, low short circuit current (I_{SC}), and an erratic curve shape was deemed flooded.

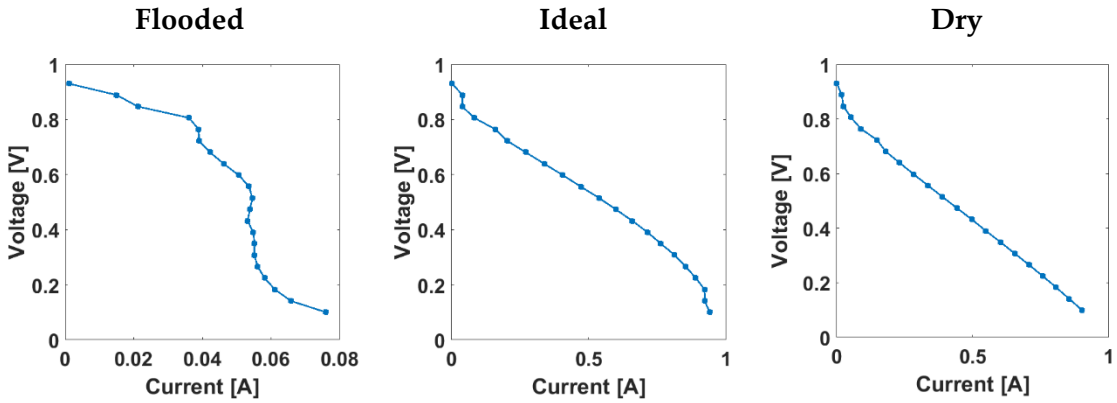

(a) (b) (c)

Figure 25: Example I-V curves for a PEM fuel cell in a Flooded (a), Ideal (b), and Dry (c) state. Note the sharp drop in voltage at low current in the flooded state ($I_{SC} \sim 0.08$ A compared to $I_{SC} \sim 1$ A).

8.5 PROX Fuel Cell Combined Performance

Two tests were performed with a PROX and PEM fuel cell combined system. The first test shown in Figure 26 shows a relatively well water-managed system over a shorter period of time. It shows that prior to connecting the two systems the PROX catalyst was converting ~99.9% (<10 ppm) of CO to CO_2 and the fuel cell maintained an average power output of 250 mW while running on pure H_2 and air. After the PROX output gas was switched to flow through the fuel cell, the average power slowly dropped to 240 mW and stayed stable, a variation of only ±1 mW, at this level for 145 minutes. At that time the gas was switched so that the output gas from the PROX would flow to the GC. No drop in PROX performance was observed after the combined test.

The fuel cell was run with pure H_2 and air again and the power recovered to its original 250 mW. The 4% relative decrease in power seems to match very closely with the 30% CO_2 dilution case observed in Figure 24. This would suggest that the decrease in power from the PROX gas is only due to the dilution from the presence of CO_2 gas, which reaches concentrations of ~25%.

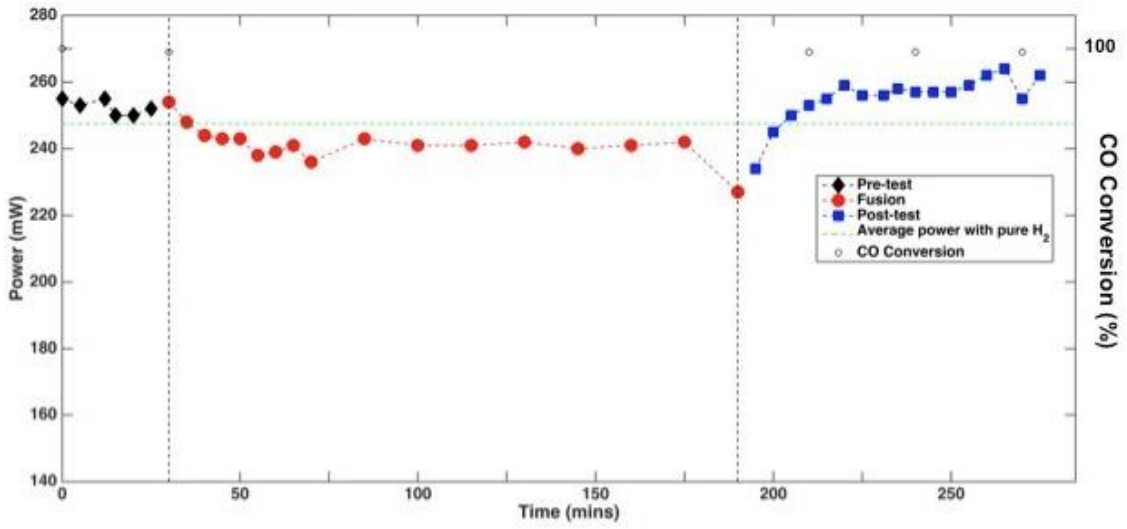

Figure 26: Properly water managed PROX and PEM fuel cell combined system.

The second test, shown by Figure 27 with details presented in Table 5, shows the importance of good water management over extended periods of time. In this experiment pure H_2 was run in the fuel cell for ~4 hours. After 170 minutes of stable fuel cell operation, the transition to PROX reformate gas leads to a sharp drop in power (~11%), and ultimately flooding. This is duel to insufficent adjustments to the humidification system in response to the increased total flow rate of the new fuel source.

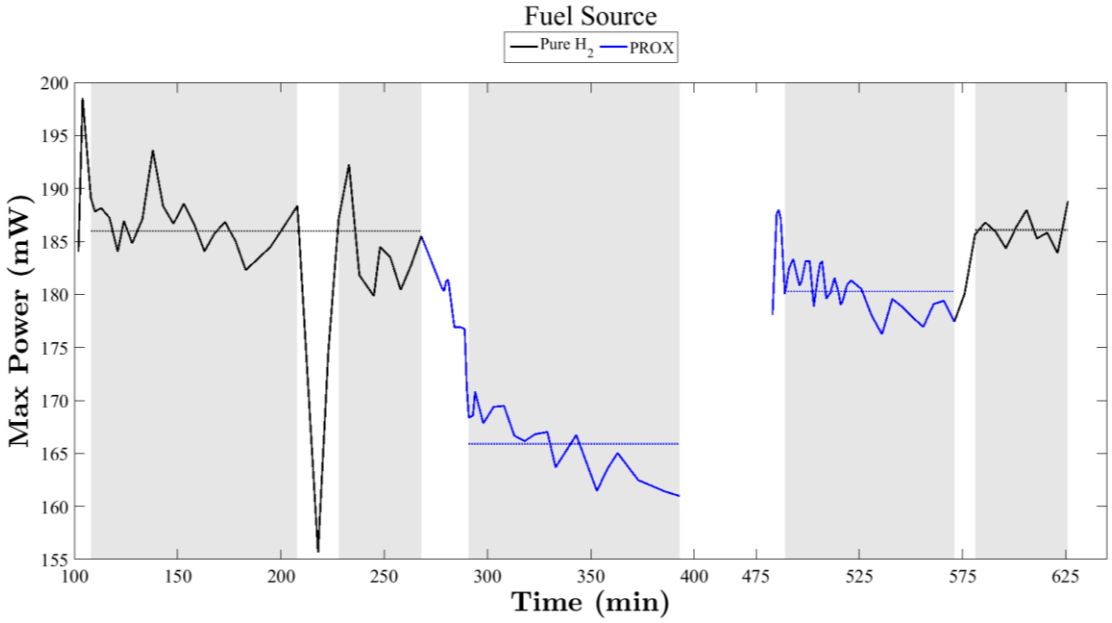

Figure 27: PEM fuel cell performance under PROX gases. Poor water management strongly degrades power (~11%) output between 300 and 400 minutes. Proper water management shows improved performance from 500-575 minutes.

By slowly drying out the cell with relatively dry PROX gas, and by carefully increasing the humidity as maximum power was reached, the fuel cell is able to reach a much higher power level while still operating under PROX gas. Additionally, when the fuel cell is transitioned back to pure H_2 the power returns to previous levels. This second, properly water managed PROX power level is a 3% relative decrease from pure H_2 and is in much closer accordance with the 4% relative decrease observed in the CO_2 dilution tests, and the first PROX fuel cell combined test.

8.6 Fuel Cell Behavior Model

Based on the conceptual model for the practical operation of a PEM fuel cell presented in section 7, it is clear that only two processes are able to bring a gas-fed PEM

fuel cell from non-ideal conditions to ideal conditions. Either $\eta < 1$ for a partially flooded state, or $\eta > 1$ for a partially dried state. However, the characteristic curves for $\eta > 1$ clearly show that the ideal physical state is reached during unstable process conditions of $\eta > \eta_i > 1$, and that the system quickly moves away from the ideal state. By comparison, approaching $\eta = 1$ from below given an initially flooded state can reach ideal physical conditions and a stable process state simultaneously, without intervention. The system is also much slower to move away from a nearly ideal state if η approaches, but ultimately fails to reach 1. Additionally, if $\eta = 1$ before $t = t_{ideal}$, either $\dot{\mathcal{L}}_{out}$ can be increased by increasing gas flowrate or $\dot{\mathcal{L}}_{Prod}$ can be reduced by reducing inlet gas humidity. These actions, together and individually, reduce η and allows the remaining excess water to be removed in a controlled manner. If the ultimate goal is to reliably and in a controlled manner reach a stable maximum power, this model would suggest it is best to begin from a partially flooded physical state and perform a drying process of $\eta < 1$.

This theory is supported by experimental observation. Comparing Figures 28 and 29 shows how slowly increasing water bath temperature in conjunction with rising power output can lead to high stable power. In Figure 28 the fuel cell is slowly brought out of a partially flooded state with 170 mW maximum power and a water bath temperature of 65 °C to a near-ideal state of 270-275 mW maximum power at a water

bath temperature of 77-78 °C. The water bath is adjusted such that the power curve follows a gentle and consistent approach to maximum power.

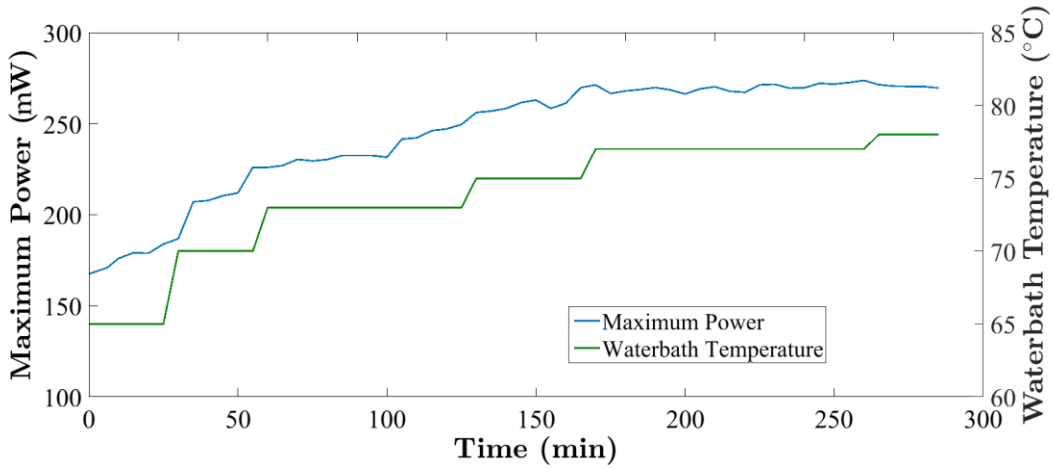

Figure 28: Properly water managed PEM fuel cell brought from a partially flooded state to a near-ideal state by a controlled drying process. Note the smooth predictable curve slowly approaching maximum power of ~275 mW.

Looking at Figure 29, it is possible to see how not raising the water bath temperature along with the performance of the fuel cell leads to sharply growing, but unstable, increases in power. This is especially clear from the power curve between 0 and 50 minutes and between 50 and 100 minutes. By maintaining a water bath temperature of just 70 °C at a power level over 250 mW, the system quickly dries. A similar maximum power of 279 mW is reached briefly, but the system is unable to sustain that power. By the time the water bath temperature is increased, the system has already dried out to well outside ideal conditions. The characteristic of sharply increasing power seen in sections of Figure 29 match the predictions of the fuel cell behavior model. Likewise the possibility of slowly approaching maximum power with

careful control of the input humidity level also matches the prediction that it is possible to reach a near-ideal state by starting with $\eta_i < \eta_{ideal}$, but augmenting the natural increase of η by increasing inlet humidity leading to an augmented increase in $\mathcal{L}_{Prod}$, eventually bringing the η curve into the stable blue regime.

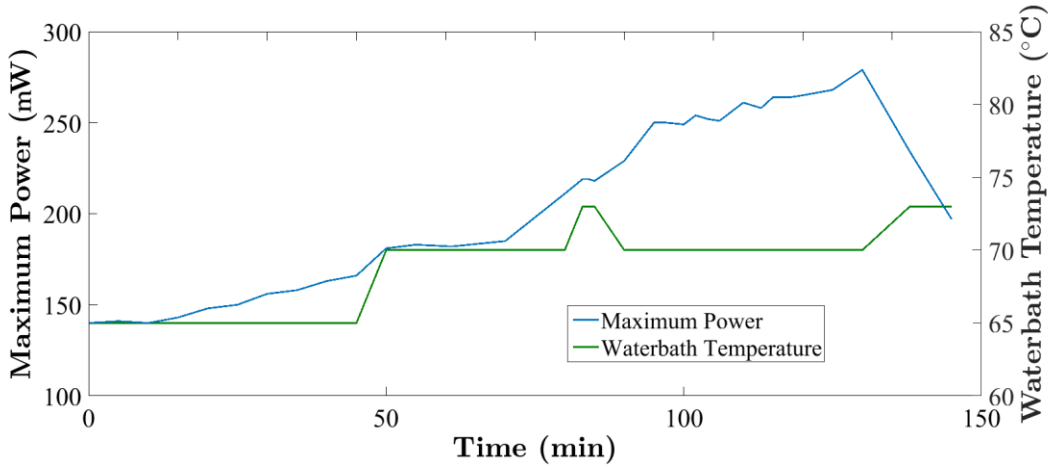

Figure 29: Poorly water managed PEM fuel cell brought from a partially flooded state through ideal and into a dry state.

9. Conclusions

The results of this study clearly show that it is possible to achieve temperatures greater than 250 °C using an advanced ETC under non-concentrated irradiation. This performance is possible with modern absorber materials, novel construction techniques, and a high-quality vacuum insulation. The thermal performance of the collector is much closer to the performance of parabolic trough collectors than previously predicted [11, 14], with operating temperatures at least 70 °C higher than previous ETC collectors at comparable efficiencies and irradiance [19].

These results have also shown that the outlet gas temperature is not limited by the heat transfer to the fluid, or the thermal conductivity of the collector material, but by the energy absorbed by the absorber coating and the flow rate of the fluid.

This claim is supported by two observations, first, that the fluid in the collector reaches maximum temperatures shortly after entering the collector, and second, that the fluid in the collector can be described analytically by a constant heat flux hypothesis. Based on this realization, copper's high thermal conductivity is no longer an advantage in high-temperature ETCs operating near stagnation temperature. A less expensive, more easily manufactured material, such as stainless steel, could be used instead. Conversely, a copper design with large collecting surfaces, but shorter piping could be used in applications where size and weight are of paramount importance, e.g. spacecraft and extraterrestrial rovers.

The collector is also shown to be a viable source of heat for the reforming of methanol into hydrogen. Maximum hydrogen production reached 66.2 ml/min STP. If the absorber area is considered this equates to a hydrogen flow rate of over 6.6 l/(min·m^2). Based on the LHV of hydrogen, the designed solar collector generates 1088 W of hydrogen per m^2 collector area under 974 W/m^2 solar illumination. . When compared to other renewable energy technologies, the current solar collector performs very well. The maximum recorded total chemical efficiency of 42.4% greatly exceeds the efficiency of commercial hydrogen production by hydrocarbon fuel reforming.

Finally, the successful operation of a PEM fuel cell off of simulated reformate gas through the use of a PROX catalyst demonstrates the possibility of combining these two technologies, solar thermal methanol-steam reformers and PEM fuel cells. The PROX catalyst was shown converting ~99.9% (<10 ppm) of CO to CO_2. The presence of CO_2 diluent in the fuel gas only decreased power output from a properly water managed fuel cell by ~4%. Most importantly, no degradation of the fuel cell occurred while operating under PROX produce gas for extended periods of time.

The critical importance of proper water management has also been demonstrated. Water management has been a major stumbling block for widespread PEM fuel cell adoption, and is a focus of intense research. It has been shown to dramatically reduced power output and decrease the stability of PEM fuel cell operation. With the goal of improving the performance of PEM fuel cells in laboratory

conditions, the author has proposed a conceptual model of fuel cell behavior for experimentalists. This model, based on experimental observation, describes a mass balance for water in the cathode side GDL. It suggests that to bring a PEM fuel cell to maximum power in a reliable and controlled manner it is best to begin from a partially flooded physical state and perform a drying process of $\eta < 1$. It is the author's hope that this model will improve the performance of reliability of PEM fuel cells for other experimentalists.

Based on the results of these experiments, a hybrid PEM fuel cell system based on a novel non-concentrating, intermediate-temperature solar collector performing methanol-steam reformation would be extremely energy efficient. Compared to photovoltaic systems currently available, the solar-to-electric energy conversion of the presented solar hydrogen reformer in combination with a conventional low temperature fuel cell (hydrogen-to-electric efficiency >55% [22]) exceeds 45% and is comparable to the world's best photovoltaic cells at laboratory scale. Moreover, a PROX catalyst could be used to remove CO from the reformate gas, preventing the immediate poisoning of the PEM fuel cell. This impressive level of performance could be further improved by optimizing the catalyst loading with respect to the collector size and by reducing the radiative heat losses due to emission from top- and bottom-sides of the collector, which further heat transfer analysis of the ETC shows accounts for 45% of the heat losses.

Reference Tables

Table 1: Material properties for the analytical model

Property	Water		Methanol		Units	Source
	77°C	277°C	77°C	277°C		
Thermal Conductivity (K)	0.0252	0.0384	0.0212	0.0422	W/m*K	[90]
Density (ϱ)	0.5925	0.4183	1.1478	0.74398	Kg/m^3	[90]
Viscosity (μ)	1.23ee-5	1.83ee-5	1.125ee-5	1.725ee-5	Pa*S	[90]
Kinematic Viscosity (ν)	2.076ee-5	4.375ee-5	9.8ee-6	2.32ee-5	m^2/S	Calculated
Specific Heat, pressure (C_p) (Non-Linear)	37.3	35.9	72.8	62.18	J/K*mol	[90]
Molar Mass	18.015		32.042		g/mol	[90]
ε/k_b (Sutherland Constant)	809.1		481.8		K	[91]

Table 2: Thermal conductivity of gas phase mixture

$m_2 = 2C^3 - 3C^2 + 1$	Values
C	0.602
A'_{12}	0.85805
A'_{21}	0.920731
λ_1	0.0443646
λ_2	0.4049
ν	9.12663
$\lambda = K_{gas}$	0.113077 @550K 0.024 @350K

Source: Dul'nev and Zarichnyak [81]

Table 3: Geometric, operational and material properties of solar collector

A_{apt}	144	cm²	-	L_o	1.0	mm	-
A_{coll}	100	cm²	-	L_ss	65.0	mm	-
D_o	6.5	mm	-	LHV_{CH_3OH}	638.6	kJ/mol	-
D_i	4.0	mm	-	LHV_{H_2}	244.0	kJ/mol	-
D_b	180	mm	-	$T_{b,o}$	323	K	-
I	1000	W/m²	-	T_g	323	K	-
$\bar{h}_{react}$	49.2	kJ/mol	[74]	T_{in}	351	K	-
k_b	15.3	W/(m K)	[92]	T_∞	300	K	-
k_{Cu}	393.0	W/(m K)	[92]	α_{sol}	0.95	-	[93]
k_o	0.5	W/(m K)	[94]	ε_{IR}	0.10	-	[95]
k_{ss}	15.75	W/(m K)	[92]	ε_{AL}	0.08	-	[92]
L_b	12.0	mm	-	τ_g	0.90	-	[96]
L_{Cu}	25.0	mm	-				

Table 4: Effect of CO_2 diluted feed gas on PEM fuel cell performance.

%CO_2 Dilution	Average Maximum Power ± 95% conf. interval [mW]	Elapsed Time [Min]	Std. Dev. [mW]	Sample Count
1st Pure H_2	272.02 ± 0.65	45	1.02	12
10% CO_2	271.20 ± 0.54	52	0.94	14
20% CO_2	269.33 ± 0.77	84	1.83	24
30% CO_2	261.93 ± 0.69	110	1.74	27
2nd Pure H_2	277.77 ± 0.64	17	0.96	11

Table 5: Effect of water management on combined PROX-PEM fuel cell performance.

Fuel Source	Average Maximum Power ± 95% confidence interval [mW]	Elapsed Time [Min]	Std. Dev. [mW]	Sample Count
1st Pure H_2	185.99 ± 0.43	170	1.14	29
1st PROX	165.91 ± 1.51	102	3.04	18
2nd PROX	180.28 ± 0.73	87	1.95	30
2nd Pure H_2	186.08 ± 1.08	45	1.5	10

Appendix A

The coefficients A'_{12} and A'_{21} are adjustment parameters that account for the exchange of intermolecular energy, and are given by

$$A'_{12} = \frac{\gamma_{12}}{\gamma_1}\left(\frac{\sigma}{\sigma_1}\right)^2 \sqrt{\frac{M_1+M_2}{2M_2}}, \tag{A1}$$

$$A'_{21} = \frac{\gamma_{12}}{\gamma_2}\left(\frac{\sigma}{\sigma_2}\right)^2 \sqrt{\frac{M_1+M_2}{2M_1}}, \tag{A2}$$

$$\gamma_1 = 1 + \frac{S_1}{T}, \quad \gamma_2 = 1 + \frac{S_2}{T}, \quad \gamma_{12} = 1 + \frac{S_{12}}{T}, \tag{A3}$$

$$S_{12} = 0.73\sqrt{S_1 S_2}, \tag{A4}$$

$$\sigma = 0.5(\sigma_1 + \sigma_2). \tag{A5}$$

where σ_i and M_i are the collision diameters and molecular mass of individual components, and the Sutherland constants, S_i, characterize the forces of intermolecular interaction. The values of all parameters used for the calculation of the fluid thermal conductivity are given in Table 1.

References

1. Real, D., et al., *Novel non-concentrating solar collector for intermediate-temperature energy capture.* Solar Energy, 2014. **108**(0): p. 421-431.

2. Real, D., I. Dumanyan, and N. Hotz, *Renewable hydrogen production by solar-powered methanol reforming.* Submitted for publication, 2015.

3. Shodiya, T., et al., *Novel nano-scale Au/alpha-Fe_2O_3 catalyst for the preferential oxidation of CO in biofuel reformate gas.* Journal of Catalysis, 2013. **300**: p. 63-69.

4. Delucchi, M.A. and M.Z. Jacobson, *Providing all global energy with wind, water, and solar power, Part II: Reliability, system and transmission costs, and policies.* Energy Policy, 2011. **39**(3): p. 1170-1190.

5. Jacobson, M.Z. and M.A. Delucchi, *Providing all global energy with wind, water, and solar power, Part I: Technologies, energy resources, quantities and areas of infrastructure, and materials.* Energy Policy, 2011. **39**(3): p. 1154-1169.

6. Kalogirou, S.A., *Solar thermal collectors and applications.* Progress in Energy and Combustion Science, 2004. **30**(3): p. 231-295.

7. Sakhrieh, A. and A. Al-Ghandoor, *Experimental investigation of the performance of five types of solar collectors.* Energy Conversion and Management, 2013. **65**: p. 715-720.

8. Speyer, E., *Solar Energy Collection With Evacuated Tubes.* Journal for Engineering for Power, 1965. **87**(3): p. 270-276.

9. Fernandez-Garcia, A., et al., *Parabolic-trough solar collectors and their applications.* Renewable & Sustainable Energy Reviews, 2010. **14**(7): p. 1695-1721.

10. Quaschning, V., *Technical and economical system comparison of photovoltaic and concentrating solar thermal power systems depending on annual global irradiation.* Solar Energy, 2004. **77**(2): p. 171-178.

11. Rabl, A., *Active Solar Collectors and Their Applications*. 1985, New York: Oxford University Press. 503.

12. Grass, C., et al., *Comparison of the optics of non-tracking and novel types of tracking solar thermal collectors for process heat applications up to 300 degrees C.* Solar Energy, 2004. **76**(1-3): p. 207-215.

13. Kumar, K.R. and K.S. Reddy, *Thermal analysis of solar parabolic trough with porous disc receiver.* Applied Energy, 2009. **86**(9): p. 1804-1812.

14. Price, H., et al., *Advances in parabolic trough solar power technology.* Journal of Solar Energy Engineering-Transactions of the Asme, 2002. **124**(2): p. 109-125.

15. Eaton, C.B. and H.A. Blum, *The use of moderate vacuum environments as a means of increasing the collection efficiencies and operating temperatures of flat-plate solar collectors.* Solar Energy, 1975. **17**(3): p. 151-158.

16. Zimmerman, R.E., *Novel micro solar collector for portable hydrogen production*, in *Mechanical and Manufacturing Engineering*. 2011, University of New South Wales: Sydney, Australia. p. 102.

17. Benz, N. and T. Beikircher, *High efficiency evacuated flat-plate solar collector for process steam production.* Solar Energy, 1999. **65**(2): p. 111-118.

18. Hudon, K., et al., *Low-Cost Solar Water Heating Research and Development Roadmap*, D.o. Energy, Editor. 2012, National Renewable Energy Laboratory.

19. Zhang, X.R., et al., *A feasibility study of CO_2-based Rankine cycle powered by solar energy.* Jsme International Journal Series B-Fluids and Thermal Engineering, 2005. **48**(3): p. 540-547.

20. Zhang, X.R., et al., *Analysis of a novel solar energy-powered Rankine cycle for combined power and heat generation using supercritical carbon dioxide.* Renewable Energy, 2006. **31**(12): p. 1839-1854.

21. Quoilin, S., et al., *Techno-economic survey of Organic Rankine Cycle (ORC) systems.* Renewable & Sustainable Energy Reviews, 2013. **22**: p. 168-186.

22. Hotz, N., et al., *Exergetic analysis and optimization of a solar-powered reformed methanol fuel cell micro-powerplant.* Journal of Power Sources, 2010. **195**(6): p. 1676-1687.

23. Huber, G.W., S. Iborra, and A. Corma, *Synthesis of transportation fuels from biomass: Chemistry, catalysts, and engineering.* Chemical Reviews, 2006. **106**(9): p. 4044-4098.

24. Hong, H., Q. Liu, and H. Jin, *Operational performance of the development of a 15 kW parabolic trough mid-temperature solar receiver/reactor for hydrogen production.* Applied Energy, 2012. **90**(1): p. 137-141.

25. Lee, M.-T., et al., *Hydrogen production with a solar steam-methanol reformer and colloid nanocatalyst.* International Journal of Hydrogen Energy, 2010. **35**(1): p. 118-126.

26. Zimmerman, R.E., G. Morrison, and G. Rosengarten, *A microsolar collector of hydrogen production by methanol reforming.* Journal of Solar Energy Engineering, 2010. **132**(1): p. 5.

27. Wagar, W.R., C. Zamfirescu, and I. Dincer, *Thermodynamic analysis of solar energy use for reforming fuels to hydrogen.* International Journal of Hydrogen Energy, 2011. **36**(12): p. 7002-7011.

28. Turchi, C., *Parabolic Trough Reference Plant for Cost Modeling with the Solar Advisor Model (SAM)*, U.S.D.o. Energy, Editor. 2010, National Renewable Energy Laboratory.

29. Hotz, N., *Hybrid Solar System for Decentralized Electric Power Generation and Storage.* Journal of Solar Energy Engineering-Transactions of the Asme, 2012. **134**(4).

30. Luo, C.D. and N. Zhang, *Zero CO_2 emission SOLRGT power system.* Energy, 2012. **45**(1): p. 312-323.

31. Zhao, H. and P. Yue, *Performance analysis of humid air turbine cycle with solar energy for methanol decomposition.* Energy, 2011. **36**(5): p. 2372-2380.

32. Li, Y., N. Zhang, and R. Cai, *Low CO_2-emissions hybrid solar combined-cycle power system with methane membrane reforming.* Energy, 2013. **58**(0): p. 36-44.

33. Nathan, G.J., D.L. Battye, and P.J. Ashman, *Economic evaluation of a novel fuel-saver hybrid combining a solar receiver with a combustor for a solar power tower.* Applied Energy, 2014. **113**: p. 1235-1243.

34. Jamel, M.S., A. Abd Rahman, and A.H. Shamsuddin, *Advances in the integration of solar thermal energy with conventional and non-conventional power plants.* Renewable and Sustainable Energy Reviews, 2013. **20**: p. 71-81.

35. Gou, C., R. Cai, and H. Hong, *A novel hybrid oxy-fuel power cycle utilizing solar thermal energy.* Energy, 2007. **32**(9): p. 1707-1714.

36. Gupta, M.K. and S.C. Kaushik, *Exergetic utilization of solar energy for feed water preheating in a conventional thermal power plant.* International Journal of Energy Research, 2009. **33**(6): p. 593-604.

37. Liao, B., et al., *Solar receiver/reactor for hydrogen production with biomass gasification in supercritical water.* International Journal of Hydrogen Energy, 2013. **38**(29): p. 13038-13044.

38. Baniasadi, E., I. Dincer, and G.F. Naterer, *Exergy and environmental impact assessment of solar photoreactors for catalytic hydrogen production.* Chemical Engineering Journal, 2012. **213**: p. 330-337.

39. Hong, H., Q. Liu, and H. Jin, *Solar Hydrogen Production Integrating Low-Grade Solar Thermal Energy and Methanol Steam Reforming.* Journal of Energy Resources Technology-Transactions of the Asme, 2009. **131**(1).

40. Liu, Q., et al., *Performance analysis of a mid- and low-temperature solar receiver/reactor for hydrogen production with methanol steam reforming.* International Journal of Energy Research, 2011. **35**(1): p. 52-60.

41. Sui, J., et al., *Experimental investigation of methanol decomposition with mid- and low-temperature solar thermal energy.* International Journal of Energy Research, 2011. **35**(1): p. 61-67.

42. Joshi, A.S., I. Dincer, and B.V. Reddy, *Exergetic assessment of solar hydrogen production methods.* International Journal of Hydrogen Energy, 2010. **35**(10): p. 4901-4908.

43. Joshi, A.S., I. Dincer, and B.V. Reddy, *Solar hydrogen production: A comparative performance assessment.* International Journal of Hydrogen Energy, 2011. **36**(17): p. 11246-11257.

44. Pregger, T., et al., *Prospects of solar thermal hydrogen production processes.* International Journal of Hydrogen Energy, 2009. **34**(10): p. 4256-4267.

45. Steinfeld, A., *Solar thermochemical production of hydrogen - a review.* Solar Energy, 2005. **78**(5): p. 603-615.

46. Jiao, K. and X. Li, *Water transport in polymer electrolyte membrane fuel cells.* Progress in Energy and Combustion Science, 2011. **37**(3): p. 221-291.

47. Rayment, C. and S. Sherwin, *Introduction to Fuel Cell Technology*. 2003, University of Notre Dame. p. 156.

48. Das, P.K., X. Li, and Z.-S. Liu, *Analysis of liquid water transport in cathode catalyst layer of PEM fuel cells.* International Journal of Hydrogen Energy, 2010. **35**(6): p. 2403-2416.

49. Connors, K.A., *Chemical kinetics : the study of reaction rates in solution*. 1990, New York, N.Y.: VCH.

50. Nam, J.H. and M. Kaviany, *Effective diffusivity and water-saturation distribution in single- and two-layer PEMFC diffusion medium.* International Journal of Heat and Mass Transfer, 2003. **46**(24): p. 4595-4611.

51. Pasaogullari, U. and C.Y. Wang, *Liquid water transport in gas diffusion layer of polymer electrolyte fuel cells.* Journal of the Electrochemical Society, 2004. **151**(3): p. A399-A406.

52. Litster, S., D. Sinton, and N. Djilali, *Ex situ visualization of liquid water transport in PEM fuel cell gas diffusion layers.* Journal of Power Sources, 2006. **154**(1): p. 95-105.

53. Manke, I., et al., *Investigation of water evolution and transport in fuel cells with high resolution synchrotron x-ray radiography.* Applied Physics Letters, 2007. **90**(17): p. 3.

54. Markoetter, H., et al., *Investigation of 3D water transport paths in gas diffusion layers by combined in-situ synchrotron X-ray radiography and tomography.* Electrochemistry Communications, 2011. **13**(9): p. 1001-1004.

55. Lu, Z., et al., *Water management studies in PEM fuel cells, part III: Dynamic breakthrough and intermittent drainage characteristics from GDLs with and without MPLs.* International Journal of Hydrogen Energy, 2010. **35**(9): p. 4222-4233.

56. Li, H., et al., *A review of water flooding issues in the proton exchange membrane fuel cell.* Journal of Power Sources, 2008. **178**(1): p. 103-117.

57. Bazylak, A., *Liquid water visualization in PEM fuel cells: A review.* International Journal of Hydrogen Energy, 2009. **34**(9): p. 3845-3857.

58. Eikerling, M., *Water management in cathode catalyst layers of PEM fuel cells - A structure-based model.* Journal of the Electrochemical Society, 2006. **153**(3): p. E58-E70.

59. Eller, J., et al., *Progress in In Situ X-Ray Tomographic Microscopy of Liquid Water in Gas Diffusion Layers of PEFC.* Journal of the Electrochemical Society, 2011. **158**(8): p. B963-B970.

60. Fairweather, J.D., P. Cheung, and D.T. Schwartz, *The effects of wetproofing on the capillary properties of proton exchange membrane fuel cell gas diffusion layers.* Journal of Power Sources, 2010. **195**(3): p. 787-793.

61. Krueger, P., et al., *Synchrotron X-ray tomography for investigations of water distribution in polymer electrolyte membrane fuel cells.* Journal of Power Sources, 2011. **196**(12): p. 5250-5255.

62. LaManna, J.M. and S.G. Kandlikar, *Determination of effective water vapor diffusion coefficient in pemfc gas diffusion layers.* International Journal of Hydrogen Energy, 2011. **36**(8): p. 5021-5029.

63. Luo, G., et al., *Modeling liquid water transport in gas diffusion layers by topologically equivalent pore network.* Electrochimica Acta, 2010. **55**(19): p. 5332-5341.

64. Nishida, K., et al., *Measurement of liquid water content in cathode gas diffusion electrode of polymer electrolyte fuel cell.* Journal of Power Sources, 2010. **195**(11): p. 3365-3373.

65. Zhou, P. and C.W. Wu, *Liquid water transport mechanism in the gas diffusion layer.* Journal of Power Sources, 2010. **195**(5): p. 1408-1415.

66. Owejan, J.P., et al., *Effects of flow field and diffusion layer properties on water accumulation in a PEM fuel cell.* International Journal of Hydrogen Energy, 2007. **32**(17): p. 4489-4502.

67. Carton, J.G., et al., *Water droplet accumulation and motion in PEM (Proton Exchange Membrane) fuel cell mini-channels.* Energy, 2012. **39**(1): p. 63-73.

68. Lu, Z., et al., *Water management studies in PEM fuel cells, part IV: Effects of channel surface wettability, geometry and orientation on the two-phase flow in parallel gas channels.* International Journal of Hydrogen Energy, 2011. **36**(16): p. 9864-9875.

69. Manso, A.P., et al., *Influence of geometric parameters of the flow fields on the performance of a PEM fuel cell. A review.* International Journal of Hydrogen Energy, 2012. **37**(20): p. 15256-15287.

70. Yousfi-Steiner, N., et al., *A review on PEM voltage degradation associated with water management: Impacts, influent factors and characterization.* Journal of Power Sources, 2008. **183**(1): p. 260-274.

71. Mädler, L., et al., *Controlled synthesis of nanostructured particles by flame spray pyrolysis.* Journal of Aerosol Science, 2002. **33**(2): p. 369-389.

72. Stark, W.J., et al., *Flame synthesis of nanocrystalline ceria-zirconia: effect of carrier liquid.* Chemical Communications, 2003(5): p. 588-589.

73. Hotz, N., et al., *Syngas production from butane using a flame-made $Rh/Ce_{0.5}Zr_{0.5}O_2$ catalyst.* Applied Catalysis B-Environmental, 2007. **73**(3-4): p. 336-344.

74. Lim, E., et al., *Flame-Made $CuO/ZnO/Al_2O_3$ Catalyst for Methanol Steam Reforming.* submitted for publication, 2014.

75. Renon, H. and J.M. Prausnitz, *Liquid-Liquid and Vapor-Liquid Equilibria for Binary and Ternary Systems with Dibutyl Ketone, Dimethyl Sulfoxide, n-Hexane, and 1-Hexene.* Industrial & Engineering Chemistry Process Design and Development, 1968. **7**(2): p. 220-225.

76. Renon, H. and J.M. Prausnitz, *Local compositions in thermodynamic excess functions for liquid mixtures.* AIChE Journal, 1968. **14**(1): p. 135-144.

77. Renon, H., C.A. Eckert, and J.M. Prausnitz, *Molecular Thermodynamics of Simple Liquids. Pure Components.* Industrial & Engineering Chemistry Fundamentals, 1967. **6**(1): p. 52-58.

78. Horstmann, S., et al., *Phase equilibrium and excess enthalpy data for the system methanol+2,2′-diethanolamine plus water.* Journal of Chemical and Engineering Data, 2002. **47**(6): p. 1496-1501.

79. Moran, M.J., et al., *Fundamentals of Engineering Thermodynamics*. 2010: John Wiley & Sons.

80. *DIPPR Project 801—Evaluated Standard Thermophysical Property Values*, A.I.o.C.E.D.I.f.P. Properties, Editor. 2009.

81. Dul'nev, G.N. and Y.P. Zarichnyak, *Thermal conductivity of binary gas mixtures.* Journal of engineering physics, 1968. **15**(4): p. 972-976.

82. Nield, D.A. and A. Bejan, *Convection in Porous Media*. Fourth Edition ed. 2013, New York: Springer.

83. Bejan, A., *Convection Heat Transfer*. 4th ed. 2013, Hoboken, N.J.: Wiley.

84. Rohsenow, W.M. and H.Y. Choi, *Heat, Mass and Momentum Transfer*. 1961, Englewood Cliffs, NJ: Prentice-Hall.

85. Berg, P., et al., *Water management in PEM fuel cells.* Journal of the Electrochemical Society, 2004. **151**(3): p. A341-A353.

86. Wang, Z.H., C.Y. Wang, and K.S. Chen, *Two-phase flow and transport in the air cathode of proton exchange membrane fuel cells.* Journal of Power Sources, 2001. **94**(1): p. 40-50.

87. You, L.X. and H.T. Liu, *A two-phase flow and transport model for the cathode of PEM fuel cells.* International Journal of Heat and Mass Transfer, 2002. **45**(11): p. 2277-2287.

88. Anderson, R., et al., *A critical review of two-phase flow in gas flow channels of proton exchange membrane fuel cells.* Journal of Power Sources, 2010. **195**(15): p. 4531-4553.

89. Tuber, K., D. Pocza, and C. Hebling, *Visualization of water buildup in the cathode of a transparent PEM fuel cell.* Journal of Power Sources, 2003. **124**(2): p. 403-414.

90. *NIST/TRC Web Thermo Tables (WTT)*, in *NIST Standard Reference Subscription Database 3 - Professional Edition*, K. Kroenlein, et al., Editors., National Institute of Standards and Technology: Gaithersburg MD.

91. Cussler, E.L., *Diffusion : Mass Transfer in Fluid Systems*. 2009, Cambridge, GBR: Cambridge University Press.

92. Incropera, F.P., et al., *Introduction to Heat Transfer*. 7th Edition ed. 2011: John Wiley and Sons.

93. Almeco, *TiNOX, Energy Cu Selective Absorber*. Datasheet.

94. Darcoid, *FF580-75*. Datasheet.

95. Gu, X.G., et al., *Thermal analysis of a micro solar thermal collector designed for methanol reforming.* Solar Energy, 2015. **113**: p. 189-198.

96. Larson Electronic Glass, *7052 Glass*. Datasheet.

Biography

Daniel Real was born on April 21, 1989 in Raleigh, North Carolina and was raised in Atlanta Georgia. He attended Oxford College of Emory University, and Emory University. He received a Bachelor's of Science in Physics from Emory University in 2011, graduating Magna Cum Laude. In 2011 he received the James B. Duke Graduate Fellowship to attend Duke University. His first paper was published in *Solar Energy*, "Novel non-concentrating solar collector for intermediate-temperature energy capture". He has been awarded an NC Space Grant Graduate Research Fellowship, an NSF Graduate Research Fellowship Honorable Mention, and multiple best poster awards. He is a member of Phi Beta Kappa, Phi Theta Kappa, and Sigma Pi Sigma. He has volunteered as a member of the Mechanical Engineering and Materials Science Graduate student counsel, where he was chair of graduate student seminars since from 2014 to 2015.